

From Detection to Recovery

Operational Analysis on LLM Pre-training with 504 GPUs

Lablup Technical Report

Lablup Inc.*

Abstract

Large-scale AI training is now fundamentally a distributed systems problem, and hardware failures have become routine operating conditions rather than rare exceptions [1, 2]. Publicly available operational evidence from production training clusters, however, remains limited. This technical report presents an empirical analysis of a 63-node NVIDIA B200 production cluster (504 GPUs), using 55 days of Prometheus time-series data and 73 days of operational logs covering 224 multi-node training sessions.

The report is based on a cross-organizational operating environment in which five parties (SKT, Upstage, Lablup, NVIDIA Korea, and VAST Data) share a unified monitoring pipeline. We document how this arrangement enabled the joint diagnosis of a 60-node-scale storage I/O bottleneck that did not appear in 2–4-node tests, illustrating a production-scale phenomenon that no single team could have isolated independently.

Using metrics collected during a months-long pre-training campaign, we perform three quantitative analyses that together yield four findings. First, for failure precursor detection, statistical analysis over 751 Prometheus metrics and 10 XID-identified GPU failures achieves a 10/10 detection rate, 2/10 pre-XID detection, and approximately 0.84 false positives per day. No single metric is consistently dominant across failure types, which motivates a multi-signal detection strategy. Second, for checkpoint I/O profiling, analysis of 523 checkpoint events traces the save/load path from GPU VRAM to the NFS server and attributes the “bandwidth paradox”—only 1.4–10.4% utilization of 200 Gbps RoCE bandwidth—to saturation of the 128-slot NFS RPC layer. Third, for multi-node failure response, we find both a concentrated node-exclusion distribution, in which the top 3 of 63 nodes account for more than 50% of all exclusions, and an auto-retry chain success rate of 33.3% over 12 chains (73 attempts total), 2.7× higher than the 12.5% rate observed for manual recovery; the median automatic retry interval is 11 minutes (IQR 10–11 min).

All analyses are grounded in production infrastructure that provides workload management at the session level, GPU-centric scheduling, and unified observability.

*Please cite this work as “Lablup Inc. (2026)”. Full author list appears in Section D. For inquiries, contact us at <https://www.lablup.com/contact>.

Contents

1	Introduction	4
1.1	Background	4
1.2	Problem Definition	4
1.3	Contributions	5
2	Failure Modes in Large-Scale Training	5
2.1	Frequent Failure Characteristics of Large-Scale Training	5
2.2	Failure Characteristics of Large-Scale Clusters	6
2.3	XID Error Classification and Recovery Strategies	8
3	Operational Infrastructure	8
3.1	Production Cluster	9
3.2	Session Abstraction	10
3.3	Sokovan Scheduler	10
3.4	Multi-Layer Monitoring	11
3.5	Cross-Organizational Operational Setting	12
4	Operational Data Analysis	12
4.1	Failure Detection and Precursor Analysis	13
4.1.1	Analysis Scope and Failure Classification	13
4.1.2	Precursor Patterns by Failure Type	13
4.2	Checkpoint Save and Recovery: Storage Bottleneck Analysis	16
4.2.1	Training I/O Profile and Checkpoint Interval	16
4.2.2	Failure Cost and Checkpoint Interval	18
4.2.3	Restart Loading Time and Bandwidth Utilization	19
4.2.4	Checkpoint Data Path: From GPU to NFS	20
4.2.5	NFS RPC Bottleneck: Resolving the Bandwidth Paradox	23
4.3	Failure Patterns and Automated Recovery	24
4.3.1	Node Exclusion Patterns	24
4.3.2	Auto-Retry Chain Analysis	26
4.3.3	Retry Interval Predictability	28
4.3.4	Success Rate Comparison and Downtime Reduction	29
4.3.5	Structural Failures and Auto-Retry Limits	30
5	Limitations	31
6	Related Work	31
7	Conclusion	31
7.1	Summary of Key Findings	32
7.2	Future Work	32
A	System Architecture Details	38
A.1	Multi-Layer Health Checks	38
A.2	Unified Storage Architecture	38
B	Glossary	39
C	GPU Monitoring Dashboard	42

1 Introduction

1.1 Background

Once model sizes exceed 100 billion parameters, training becomes a long-running distributed systems exercise rather than an isolated algorithmic workload. A single run can require hundreds of GPUs operating in lockstep for weeks, which invalidates the classical assumption of stable underlying infrastructure. The Solar Open technical report [3], for example, documents the following conditions during training of a 102-billion-parameter MoE model on a 60-node NVIDIA B200 cluster:

- Persistent compatibility issues during early B200 deployment, including graph compilation failures caused by the absence of CUDA 13.0 support in Triton and ScaledDotProductAttention backend errors ([3], Section 3.3.4)
- Performance degradation during multi-node scaling with FSDP2: TPS dropped from 5,500 to 4,267 when scaling from 16 to 60 nodes, requiring iterative tuning via HSDP to recover throughput ([3], Section 3.3.2)
- Performance instability caused by router dtype mismatch after sigmoid operations (13.7% speedup upon fix), unnecessary group GEMM padding overhead (14.5% performance improvement with fast-path bypass), and gradient norm instability due to excessive token batching ([3], Sections 3.3.3–3.3.4)
- Data loading bottleneck where I/O lock contention caused initialization to take over 8 hours, resolved by file-level Arrow sharding that reduced startup time to approximately 8 minutes ([3], Section 3.3.5)

These examples show that large-scale training must be managed as a systems problem in which interruptions, restarts, and performance variability are expected. Infrastructure and orchestration therefore deserve the same analytical attention as model design.

1.2 Problem Definition

Large-scale AI infrastructure faces three tightly coupled challenges.

Low resource utilization. Despite GPUs being expensive and scarce resources, actual utilization often remains at low levels due to static allocation policies and conservative operational practices. An analysis of Microsoft’s production GPU clusters reported median GPU utilization of approximately 52% [4].

Scalability–stability conflict. As cluster scale increases, hardware failures, network latency issues, and driver errors become more frequent, raising the likelihood that training jobs are completely interrupted. Meta reported that hundreds of unexpected interruptions occurred during the 16K-GPU Llama 3 pre-training, with the majority attributable to hardware issues [1] (we discuss this in detail in Section 2).

Operational complexity. The diversity of framework, driver, and library combinations undermines environment reproducibility and introduces variability in experiment quality. MegaScale’s deployment experience confirms that managing such software heterogeneity at scale constitutes a persistent operational burden [5].

These challenges reinforce one another and therefore require an integrated infrastructure-level response.

1.3 Contributions

This report analyzes data collected from August through December 2025 during Solar Open training on a production NVIDIA B200 cluster (63 nodes, 504 GPUs). Our contributions fall into two groups: one research-setting contribution that establishes the operational environment for the study, and four quantitative findings derived from production data.

Research setting.

- (S1) **Cross-organizational operating environment.** We document the five-organization collaborative environment (SKT, Upstage, Lablup, NVIDIA Korea, VAST Data) and a 60-node-scale storage I/O bottleneck that emerged only at production scale, illustrating that large-scale training phenomena cannot be predicted from 2–4-node pre-tests and that single-team monitoring is structurally insufficient for root-cause identification at this scale (Section 3.5).

Quantitative findings.

- (F1) **Failure precursor detection.** For 10 XID-identified GPU failures, we apply statistical analysis to 751 Prometheus metrics. Multi-signal statistical detection achieves a 10/10 detection rate, 2/10 pre-XID detection rate, and approximately 0.84 false positives per day. We confirm that no single metric is consistently distinctive across failure types and report ongoing time-series ML modeling to improve the pre-XID detection rate (Section 4.1).
- (F2) **Full-stack profiling of checkpoint I/O.** From 55 days of operational data, we provide a quantitative analysis of 523 checkpoint events and profile the save/load path from GPU VRAM to the NFS server using Prometheus metrics. The analysis identifies that the root cause of the bandwidth paradox—where only 1.4–10.4% of 200 Gbps RoCE bandwidth is used—lies in the saturation of 128 slots in the NFS RPC protocol layer (Section 4.2).
- (F3) **Analysis of node exclusion patterns.** Analyzing node exclusion frequencies across 224 multi-node training sessions over 73 days, we identify a concentrated distribution—the top 3 of 63 nodes (gpu074, gpu119, gpu086) account for more than 50% of all exclusions—and discuss its operational implications (Section 4.3.1).
- (F4) **In-depth evaluation of automated failure recovery.** Analyzing 12 auto-retry chains (73 attempts in total), we quantify chain success rate (33.3%, $2.7\times$ higher than manual recovery), retry-interval predictability (median 11 min, IQR 10–11 min), and downtime reduction (median 1.9 h vs. 3.3 h manual). We also analyze the limits in structural failures (Section 4.3.2).

2 Failure Modes in Large-Scale Training

This section characterizes failures at cluster scale and derives the corresponding infrastructure requirements from recent production reports [3, 1, 5].

2.1 Frequent Failure Characteristics of Large-Scale Training

Failures are an expected property of large-scale training environments [2, 1]. Failure frequency rises with cluster scale. Meta reported 419 unexpected interruptions during the 54-day pre-training of the Llama 3 405B model on a cluster of up to 16,384 H100 GPUs [1]. Meta’s RSC-1 and RSC-2 clusters, which together comprise roughly 24,000 A100 GPUs, likewise exhibited failure frequencies that scaled with cluster size [2]. Erben et al. further estimated that, at current GPU failure rates, a 100,000-GPU cluster would experience a failure roughly every 30 minutes [6].

2.2 Failure Characteristics of Large-Scale Clusters

In large-scale distributed training, faults originating in a small number of nodes can affect the entire cluster. Because multi-node training synchronizes workers tightly, a single GPU failure or communication error can interrupt the whole job. A common operational response is *node exclusion*, that is, withholding specific nodes from multi-node allocations. Node exclusion reflects a mixture of confirmed hardware failures, observed performance degradation, and preventive operator judgment, and therefore does not map one-to-one to hardware defects [2]. Section 4.3.1 analyzes node exclusion patterns in our production cluster in detail.

To place our cluster’s failures in context, we compare them with large-scale references. Table 1 reproduces the failure taxonomy used by ByteDance’s Minder system [7], which classifies failures in production GPU clusters of roughly 1,500 nodes (more than 10,000 GPUs). Minder relies on system-wide metrics that include CPU and GPU utilization, PFC counters, network throughput, disk I/O, and memory.

Table 1: Failure taxonomy of the ByteDance Minder system

Category	Failure Type	Description	Ratio (%)
Intra-host HW	ECC errors	GPU memory data corruption or loss	38.9
	PCIe downgrading	Reduced transfer rate due to PCIe link failure	6.6
	NIC dropout	NIC unrecognized by OS	5.7
	GPU card dropout	GPU card detached from host	2.0
	NVLink errors	NVLink interconnect failure between GPUs	1.7
	AOC errors	Active optical cable errors	0.9
	Subtotal		55.8
Intra-host SW	CUDA runtime errors	CUDA program execution failure	14.6
	GPU execution errors	Page faults, OOM, or GPU hangs	7.7
	HDFS errors	Checkpoint I/O errors	5.7
	Subtotal		28.0
Inter-host NW	Machine unreachable	SSH or VM service failure	6.0
	Subtotal		6.0
Others	—	—	10.3

Based on Minder [7] Table 1 and Appendix A. Observed in ByteDance production GPU clusters.

While Minder classifies failures through analysis of system-wide metrics, our cluster uses *XID error codes*—numeric fault identifiers reported by the GPU driver—recorded by the NVIDIA GPU kernel driver in `dmesg` as the primary means of failure detection. Each XID code corresponds to a specific failure type (e.g., XID 79 = GPU card dropout, XID 94 = ECC error, XID 145/149 = NVLink errors). The failure case analyses and node exclusion analyses presented in subsequent sections are based on these XID records.

Because the two systems differ in both monitoring approach and infrastructure configuration, their classification scopes do not fully overlap. The main differences are as follows:

- **HDFS errors:** Not directly applicable, as our cluster uses NFS (Network File System) rather than HDFS (Hadoop Distributed File System). NFS-based checkpoint I/O issues, however, are analyzed separately in Section 4.2.5.
- **PCIe downgrading:** Does not generate XID errors and manifests only as bandwidth degradation, so it falls outside the XID-based analysis scope of this report (separate bandwidth monitoring would be required).

- **NIC dropout and AOC errors:** NICs (Network Interface Cards) and AOCs (Active Optical Cables) operate outside the GPU driver layer and are not reported as XIDs, so they are excluded from this analysis (dedicated network monitoring would be required).
- **CUDA runtime errors:** As application- or framework-level errors, they are excluded from the scope of hardware failure analysis in this report.

Accordingly, the analysis in this report focuses on failures detectable via XID (GPU card dropout, ECC (Error-Correcting Code) errors, NVLink failures); failure types outside the XID scope, which would require separate monitoring infrastructure, are not covered.

Table 2 classifies the 17 failure events recorded in our cluster during the 55-day observation period by mapping XID codes to Minder failure categories.

Table 2: Failure distribution of our cluster, mapped to Minder categories

Failure Type (Minder Category)	XID Code	Count	Ratio (%)
NVLink errors	145, 149	5	29.4
ECC errors	94	2	11.8
GPU card dropout	79	2	11.8
GPU execution errors	119	1	5.9
Machine unreachable	—	2	11.8
Others (e.g., performance degradation)	—	5	29.4
Total		17	100.0

63-node cluster (504 B200 GPUs), 55-day observation period. Classified by mapping XID codes to Minder failure categories.

The two distributions differ in their dominant failure category. In Minder, ECC errors (38.9%) constitute the most frequent category, whereas in our cluster, NVLink errors (29.4%) are the most prevalent. XID codes explicitly record NVLink failures (XID 145/149), while ECC events have a small sample size due to the shorter observation period. The Others category (29.4%) includes operational-level events such as performance degradation that do not directly map to XID codes. These differences arise from variations in monitoring strategy, observation period, and workload size distribution. Section 4 analyzes individual failure cases, and Section 4.3.1 examines how these failures translate into node exclusion patterns over the observation period.

Fail-slow faults and straggler detection. The taxonomy above emphasizes *fail-stop* faults, in which a GPU or node stops functioning entirely. Our node exclusion data, however, reveals a second class of failures: nodes such as gpu074 and gpu119¹ were repeatedly excluded because their training speed had degraded. These are *fail-slow* faults, in which a component remains operational but slows down enough to impair the job. Because distributed training synchronizes workers every iteration, a single slow node can delay the entire run. Fail-slow faults are correspondingly harder to detect than fail-stop faults because they do not necessarily emit explicit error codes.

Recent production studies suggest that this pattern is widespread. Wu et al. [8] reported that, in 10,000+ GPU clusters, 59% of large-scale training jobs (512–1,024 GPUs) experienced fail-slow stragglers and suffered an average job completion delay of 34.59%. Lin et al. [9] found that 42.5% of jobs in production LLM training clusters were affected by stragglers, wasting 10.4% of total GPU hours; that study attributed the dominant causes to workload-level imbalances such as pipeline-stage skew and garbage collection pauses rather than to hardware faults.

¹In this report, “gpuXXX” denotes a node identifier within the cluster (e.g., gpu074 = node 74), while “GPU#N” denotes an individual GPU index (0–7) within a node. Each node houses 8 B200 GPUs.

In our cluster, the lack of per-iteration throughput instrumentation meant that operators could identify fail-slow nodes only after noticing speed differences across sessions. Section 7.2 outlines the monitoring extensions needed to replace this reactive process.

2.3 XID Error Classification and Recovery Strategies

NVIDIA GPUs report hardware and software errors through XID error codes [10]. Since different XID codes require fundamentally different responses, correctly classifying these codes is a prerequisite for failure attribution. Table 3 classifies the XID codes observed in the operational cluster by NVIDIA-defined resolution types.

Table 3: XID error code classification by resolution action

XID	Description	Resolution	Action
<i>Hardware action required (node/GPU reset needed)</i>			
79	GPU fell off the bus	RESTART_BM	Node reboot
119	GSP RPC timeout	RESET_GPU	GPU reset
145	NVLink RLW error	RESET_GPU	GPU reset
149	NVLink NETIR error	RESET_GPU	GPU reset
<i>Application level (process restart sufficient)</i>			
31	GPU memory page fault	RESTART_APP	Session restart
43	GPU processing halted	RESTART_APP	Session restart
94	Contained ECC error	RESTART_APP	Auto-corrected

This classification is reflected in Backend.AI’s failure handling strategy (Section 4.3). XID errors requiring hardware action (79, 119, 145, 149) trigger node isolation and session migration to spare nodes, while application-level errors (31, 43, 94) are handled through automatic retries without excluding the affected node. In practice, failure rates also depend on the system stack (OS kernel, GPU driver, firmware version) and workload intensity.

3 Operational Infrastructure

Given the failure characteristics discussed in Section 2, the infrastructure must satisfy two core requirements:

- 1. Fault tolerance through detection, isolation, and recovery:** Detection operates across multiple layers—hardware (GPU ECC errors, temperature, power), process (container status, OOM (Out of Memory)), application (training progress, loss trajectory), and network (NVIDIA Collective Communications Library (NCCL) timeouts, bandwidth degradation). Application-level concerns such as loss divergence are delegated to the training framework. When a fault is detected, the affected node or GPU is isolated from the scheduling pool to limit the scope of its impact. During recovery, the system allocates replacement resources and restarts the session, with checkpointing delegated to the training framework, minimizing total training throughput loss.
- 2. Session-level lifecycle management:** The lifecycle of a training job is managed at the session level. A session is a logical unit that spans one or more containers across multiple nodes and is tied to training state, including checkpoints and optimizer state. When a session is restarted, the job resumes from the last checkpoint. The system reliably tracks and persists state transitions to support accurate recovery and auditing.

Both requirements assume that GPUs, rather than CPUs, are the primary scheduling resource and that CPU and memory allocations are derived from GPU placement. Traditional CPU-centric orchestration does not make this assumption.

This section describes the infrastructure components that implement those requirements. The infrastructure layer sits below the training frameworks (PyTorch, DeepSpeed, Megatron-LM, and others) and provides environment provisioning, resource allocation, checkpoint storage, and failure alerting. To ground the operational analyses in Section 4, we first summarize the cluster hardware (Section 3.1), then describe the session abstraction and recovery mechanism (Section 3.2), and finally explain the multi-layer monitoring pipeline used for precursor analysis (Section 3.4). We focus on the components referenced directly in the analysis sections; further implementation details are deferred to Appendix A.

3.1 Production Cluster

The production cluster used throughout this report is a 63-node NVIDIA DGX B200 system. Table 4 summarizes the hardware configuration of the cluster.

Table 4: Production cluster hardware configuration

Component	Specification
Nodes	63 (DGX B200): 60 for training, 3 spare
GPU	8× NVIDIA B200 per node (504 total)
GPU Memory	192 GB HBM3e per GPU
System RAM	2 TiB DDR5 per node
Intra-node GPU Interconnect	5th-gen NVLink, 1.8 TB/s bidirectional
Inter-node Interconnect	8-port × 400G InfiniBand (3.2 Tbps/node)
Storage Network	200G RoCE (RDMA over Converged Ethernet)
Storage	VAST Data E-Box, 2 PiB, NFS mount

Model parameters, activations, and gradients reside in 192 GB of HBM3e per GPU [11].

During each training iteration, data traverses the following path. In the forward and backward passes, each GPU’s SMs and Tensor Cores perform computation, while the 8 GPUs within a node communicate via NVLink for tensor parallelism. Gradient synchronization (AllReduce) is carried out across all 63 nodes over InfiniBand NDR (8 ports × 400G per node); if even a single node is slow, the entire training job stalls—the straggler problem [12]. Checkpoint saves and data loading access the VAST Data NFS storage through a dedicated 200G RoCE network. These three traffic types—compute (InfiniBand), storage (RoCE), and management (Ethernet)—are physically separated to prevent mutual interference.

This communication structure forms the physical foundation for the subsequent analyses. The NFS RPC analysis in Section 4.2.5 addresses bottlenecks on the storage plane, while the precursor analysis in Section 4.1 treats InfiniBand port counters, TCP/socket metrics, and GPU telemetry (DCGM) as signals from different network planes.

The software stack running on this hardware is summarized in Table 5. The upper section lists the base container image and core libraries (CUDA, cuDNN, NCCL, PyTorch), while the lower section shows the training configuration used by the Solar Open project [3] on this cluster—parallelization strategy, batch size, sequence length progression, and precision format.

Table 5: Production training software stack

Component	Version
Base Image	NGC PyTorch 25.08
CUDA	13.0.0
cuDNN	9.12.0
NCCL	2.27.7
PyTorch	2.9.0.dev20250830+cu130
TorchTitan	(included in PyTorch nightly)
Transformers	4.55.2
Flash Attention	2.7.4.post1
Python	3.12
<i>Training Configuration (Solar Open [3])</i>	
Parallelism	HSDP (10-node sharding group \times 6 replicas)
Global Batch Size	13,440 (28 per GPU)
Sequence Length	4K \rightarrow 32K \rightarrow 100K (progressive scaling)
Precision	FP8 + bfloat16 mixed

The following subsections describe the orchestration layer’s session management and node isolation mechanisms used on this cluster.

3.2 Session Abstraction

Deep learning training workloads are stateful tasks that preserve optimizer parameters and learning rate schedules across iterations [1, 5]. Upon failure, the container is destroyed, but the training session retains all progress up to the last checkpoint. Backend.AI reflects this distinction by using *sessions*—which bundle storage volumes and lifecycle state—as the core management unit instead of containers (Table 6).

Table 6: Comparison of container and session characteristics

Property	Container	Session (DL Training)
Lifecycle	Process exit = completion	Progress to checkpoint = completion
State	Stateless by design	Stateful (optimizer, gradients)
Restart semantics	Start from scratch	Resume from checkpoint
Failure impact	Process lost	Progress since last checkpoint lost

This distinction is directly relevant to the automated recovery analysis in Section 4.3. Since “restart” means checkpoint resumption rather than starting from scratch, recovery time is determined by checkpoint loading time (median 31 minutes, Section 4.2.3).

3.3 Sokovan Scheduler

GPU allocation for sessions is handled by the Sokovan scheduler. Scheduling operates at two levels: at the cluster level, pending sessions are evaluated against resource groups to control density and priority; at the node level, NUMA-aware placement policies allocate GPUs, CPU cores, and memory from the same NUMA node (Figure 1). Co-locating resources on the same NUMA node avoids cross-NUMA-node memory access, improving throughput by up to $1.30\times$ [13].

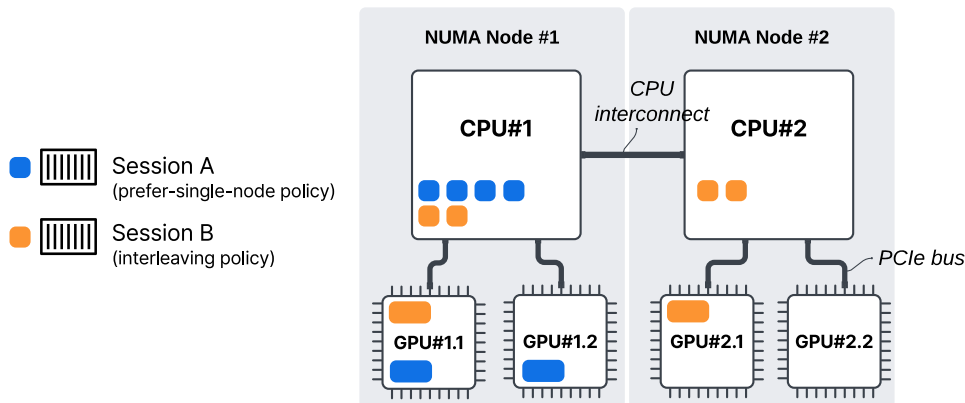


Figure 1: NUMA-aware resource allocation within a GPU server node (from [14]). Session A uses a *prefer-single-node* policy, allocating all resources from NUMA Node #1. Session B uses an *interleaving* policy, spreading resources across both NUMA nodes.

Particularly critical for distributed training is gang scheduling. A 60-node training job must allocate all participating nodes simultaneously; partial allocation causes deadlocks during NCCL initialization. Sokovan allocates all N slots or enqueues the entire request (all-or-nothing), preventing resource fragmentation where partially allocated jobs hold GPUs idle while waiting for the remaining slots. This constraint is directly related to the structural cause of auto-retry failures analyzed in Section 4.3.5—repeated failure when fewer than 60 nodes are available.

3.4 Multi-Layer Monitoring

GPU-only monitoring (DCGM) alone is insufficient to capture failure precursors. Table 7 contrasts DCGM-only monitoring with integrated multi-layer monitoring.

Table 7: Comparison of GPU-only monitoring and multi-layer monitoring

	DCGM Only	Integrated Monitoring (Scheduler + OS + DCGM)
Detection timing	After failure occurs (reactive)	Before failure occurs (precursor detection possible)
Observability scope	GPU chip state	Full stack including OS, network, and scheduler

NVIDIA DCGM provides chip-level telemetry such as GPU temperature, power, and ECC errors, but XID error codes are recorded only after the GPU has already halted. In contrast, system-level metrics (TCP socket allocation, kernel memory, interrupts) and scheduler-level metrics (async task count, RPC latency) provide pathways through which anomalies in the GPU driver or NCCL communication layer surface before they appear in GPU telemetry. Section 4.1 validates this across 10 GPU failure events.

Metric collection pipeline. The production cluster runs four Prometheus-compatible exporters per node, scraping metrics at 30-second intervals (Table 8).

Table 8: Prometheus exporters deployed per node

Exporter	Scope	Key Metrics
DCGM (Data Center GPU Manager)-exporter [15]	GPU	Utilization, temperature, power, ECC errors, NVLink, XID
node_exporter [16]	OS / Hardware	CPU, memory, disk I/O, network, InfiniBand, NFS
all-smi [17]	Cross-platform GPU	GPU power, system memory, chassis-level telemetry
Backend.AI	Scheduler	API latency, active sessions, RPC metrics

Across 63 nodes, approximately 751 unique metric names are collected in total. Of these, approximately 305 active metrics were used for failure analysis; metrics unrelated to the analysis

scope (ZFS statistics, Go runtime internals, etc.) were excluded. Continuous collection over 55 days produced approximately 126 GB of uncompressed raw telemetry, stored in VictoriaMetrics, a Prometheus-compatible time-series database.

The operational GPU monitoring dashboard that visualizes metrics from both DCGM and `all-smi` sources is presented in Appendix C (Figure 19).

3.5 Cross-Organizational Operational Setting

The cluster operates within a five-organization collaboration that includes SKT (cloud operations), Upstage (model development), Lablup (Backend.AI infrastructure), NVIDIA Korea (hardware), and VAST Data (storage). Metrics from all parties feed into a shared monitoring pipeline (Section 3.4) and can be queried on a common timeline across organizational boundaries. This shared substrate is essential for the analyses in Section 4: failures and bottlenecks that span layers can be diagnosed directly rather than reconstructed after the fact from disconnected dashboards.

An illustrative case: storage I/O at production scale. The value of this operational setting became clear during early deployment of the 60-node B200 training configuration, when a severe I/O bottleneck appeared only at production scale. Training initialization from VAST storage, which should have completed within minutes, instead took more than 8 hours while sustaining throughput far below the theoretical limit. The Solar Open pre-training report independently documented the same symptom and attributed it to I/O lock contention [3]. No single team’s local view exposed the root cause: each subsystem appeared healthy in isolation, and the bottleneck became visible only after metrics from the application, scheduler, network, and storage layers were correlated jointly.

Joint diagnosis across the model-development, infrastructure, hardware, and storage teams traced the problem to a mismatch between the expected large sequential I/O pattern and the fragmented small random I/O pattern that actually reached the storage layer, saturating the distributed metadata service. Each node’s storage NIC receive rate (approximately 4–10 GiB/s) looked unremarkable in isolation, but the aggregate access pattern generated simultaneously by 60 nodes overwhelmed the metadata path. Application-side file sharding (Arrow files partitioned by rank), combined with storage-side changes such as asynchronous deletion in place of synchronous `rm/unlink` and readahead tuning, reduced initialization time from more than 8 hours to less than 8 minutes.

Implications for the analyses that follow. Two points from this case set the methodological baseline for Section 4. First, performance characteristics observed at a 2–4-node scale do not predict behavior at 60 nodes; storage and metadata bottlenecks of this kind manifest only at production scale, so small-scale pre-tests are structurally insufficient for identifying them. Second, isolated monitoring by any single team is inadequate for root-cause identification at this scale; the shared metrics pipeline across organizations is what makes the systematic operational analysis in Section 4 tractable. The quantitative analyses that follow rest on both conditions.

4 Operational Data Analysis

This section presents three analyses of production data that together yield four quantitative findings. The overall training campaign spans 73 days, of which 55 days are covered by Prometheus time-series data. Section 4.1 analyzes cross-metric behavior at failure time using the integrated monitoring pipeline. Section 4.2 quantifies NFS storage I/O and profiles the checkpoint data path across the full stack. Section 4.3 studies response to failures in multi-node training

through node exclusion patterns and the operational effectiveness of automated recovery; this final analysis contributes two complementary findings. Together, the three analyses follow a detect \rightarrow understand \rightarrow recover progression that connects the monitoring signals in Section 3.4 to the recovery pipeline. The motivating cross-organizational debugging episode was discussed separately in Section 3.5.

4.1 Failure Detection and Precursor Analysis

The previous section described a case in which the root cause was identified only after a failure became visible. This section asks whether anomalies can instead be detected before the failure manifests.

Table 2 reports failures at the event level. For precursor analysis, we refine those records to the node \times time-point level and identify 21 failures across 14 cluster downtimes². These cases comprise 13 GPU hardware failures (10 with XID detection and 3 without), 4 fail-slow events, and 4 failures of unknown cause. We analyze the 10 cases for which XID errors immediately identified both the faulty node and the failure time (Section 4.1.1); in the remaining 11 cases, the absence of XID records made automatic localization difficult.

4.1.1 Analysis Scope and Failure Classification

Precursor analysis requires that the faulty node and time point be identified. Of the 21 failures identified above, the 10 cases with node and time point identified by XID errors were selected for analysis (Table 9). Failure types were classified based on XID error codes; when multiple XIDs occurred simultaneously in a single case, it was included in all applicable types (e.g., gpu071 falls under both NVLink and Bus Fault). All 10 cases were GPU hardware-related failures, with NVLink errors (XID 145/149) being the most frequent at 6 cases.

Table 9: Overview of 10 GPU failure cases (out of 21) for which the faulty node and time point were identified by XID errors. Failure types are classified based on XID error codes. Session elapsed time indicates the time from training session start to failure occurrence.

Node	Date	Failure Type	XID	Session Elapsed Time
gpu071	10/20	NVLink + Bus Fault	79, 145	157.6h
gpu085	10/23	NVLink Error	145, 149	0.8h
gpu122	10/23	ECC Error	94	4.7h
gpu085 [†]	10/23	NVLink Error	145, 149	0.7h
gpu116	10/25	Bus Fault + ECC	79, 94	37.8h
gpu071	11/9	NVLink + Bus Fault	79, 145	44.8h
gpu096	11/17	ECC Error	94	165.3h
gpu123	11/20	NVLink Error	145, 149	1.9h
gpu068	11/24	NVLink Error	145, 149	15.3h
gpu071	11/29	GSP RPC Timeout	119	62.1h

[†]gpu085 experienced failures in two separate sessions on the same day (10/23) and is included as independent cases.

4.1.2 Precursor Patterns by Failure Type

Because 60 nodes execute the same workload concurrently, anomaly detection can be framed as deviation from the peer distribution. We therefore test whether the faulty node’s metrics depart significantly from the distribution observed across the remaining 59 healthy nodes. The discussion below groups failures by XID code and presents representative metric patterns for each failure type. The main goal is to show that automated faulty-node detection is feasible when the failing node diverges clearly from its peers.

²Multiple nodes may experience failures simultaneously during a single downtime. For example, during the 10/23 downtime, gpu085 and gpu122 each failed independently.

NVLink-related failures (XID 145/149, 6 cases). Figure 2 shows the NVLink + Bus Fault case for gpu071 (10/20). The top panel is the count of interrupts handled by the host CPU (`node_intr_total`, 30-second counter increment), and the bottom panel is the number of currently runnable processes (`node_procs_running`, instantaneous value). For both metrics, peer nodes remain stable throughout training, while gpu071 deviates clearly at the XID time point. The interrupt count drops sharply at the XID time point from approximately 300K (peer) to around 70K–100K, consistent with no further interrupts being generated on the device after the GPU was disconnected from the bus due to the NVLink error. The number of runnable processes is comparable to peers during training but drops to 0 at the XID time point—the training worker process terminated as the GPU halted, eliminating the runnable processes themselves. A similar pattern was observed when the failure recurred on the same node on 11/9.

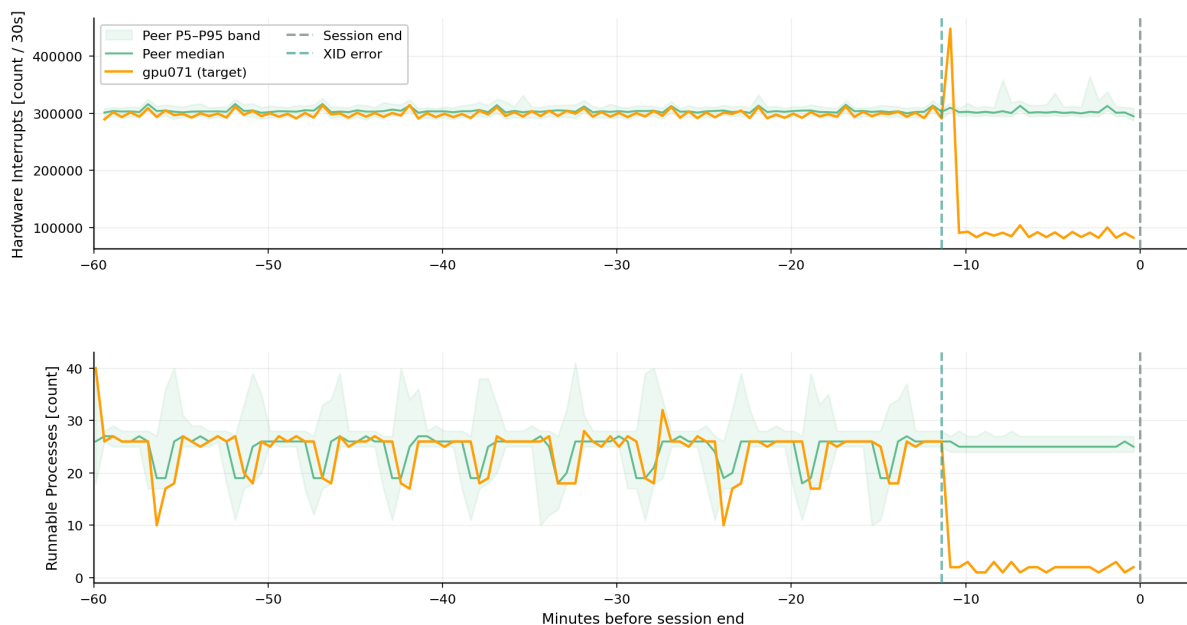


Figure 2: NVLink + Bus Fault (gpu071, 2025-10-20). Top: host CPU interrupts (`node_intr_total`, 30-second counter increment); drops sharply at XID time point from approximately 300K (peer) to about 70K–100K. Bottom: runnable process count (`node_procs_running`, instantaneous value); drops to 0 at XID time point as the worker process terminates.

ECC Error (XID 94, 3 cases). Among ECC (Error-Correcting Code) errors, XID 94 is reported on multi-bit (uncorrectable) memory faults that ECC could not correct. Single-bit correctable errors are auto-handled by ECC and not reported as XID. Figure 3 shows the ECC Error case for gpu096 (11/17). The top panel is the cumulative response time of NFS GETATTR requests (`node_mountstats_nfs_operations_response_time_seconds_total`, GETATTR operation, 30-second cumulative time), and the bottom panel is the cumulative count of page-outs from memory to disk/storage (`node_vmstat_ppgout`, 30-second counter increment). Both metrics show a clear surge on gpu096 relative to peers at the XID time point. We hypothesize that kernel-side cleanup work occurring just after the worker process terminated abnormally due to the ECC error—NFS revalidation triggered by file-handle reclamation and writeback flush of held dirty pages—led to the simultaneous surges in both metrics, though the exact causal mechanism cannot be determined from this data alone.

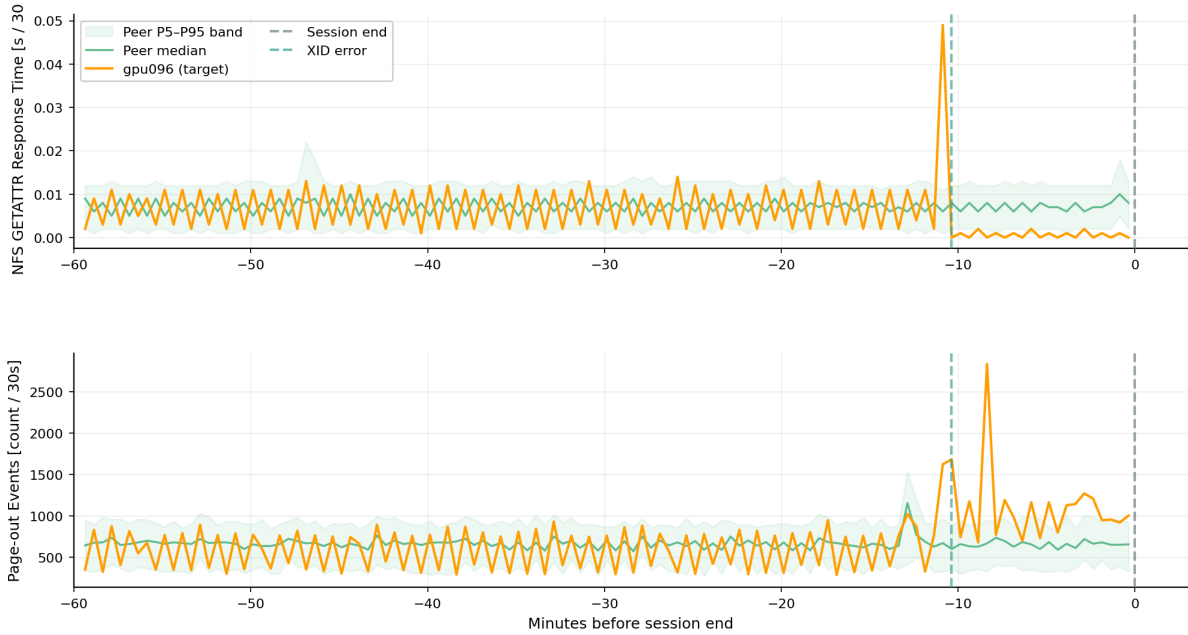


Figure 3: ECC Error (gpu096, 2025-11-17). Top: NFS GETATTR response time (`node_mountstats_nfs_operations_response_time_seconds_total`, 30-second cumulative time); surges relative to peers at XID time point. Bottom: page-out events (`node_vmstat_pgpgout`, 30-second counter increment); surges at XID time point.

The memory row remapping counter provided by DCGM can be used as an indicator for tracking long-term hardware degradation. When an ECC error occurs in GPU memory, the defective row is remapped to a spare row; uncorrectable remapping indicates a permanent defect. The top panel of Figure 4 shows the uncorrectable remapping trend for gpu122 (GPU#1). XID 94 (ECC Error) occurred simultaneously at the time points when this value increased, causing the GPU to halt. Uncorrectable remapping indicates progressing memory degradation, and when uncorrectable remappings per bank reach 8, the `ROW_REMAP_FAILURE` flag is triggered, necessitating GPU replacement [18].

The bottom panel of Figure 4 shows the correctable remapping for gpu124 (GPU#2). It accumulated at an accelerating rate up to 254 rows over 55 days; however, no uncorrectable remapping or XID errors occurred, and the GPU was ultimately replaced due to non-recognition. NVIDIA advises that correctable errors can be ignored, as hardware corrects them automatically [18]; however, a rapidly increasing trend may signal progressing memory degradation and warrant monitoring.

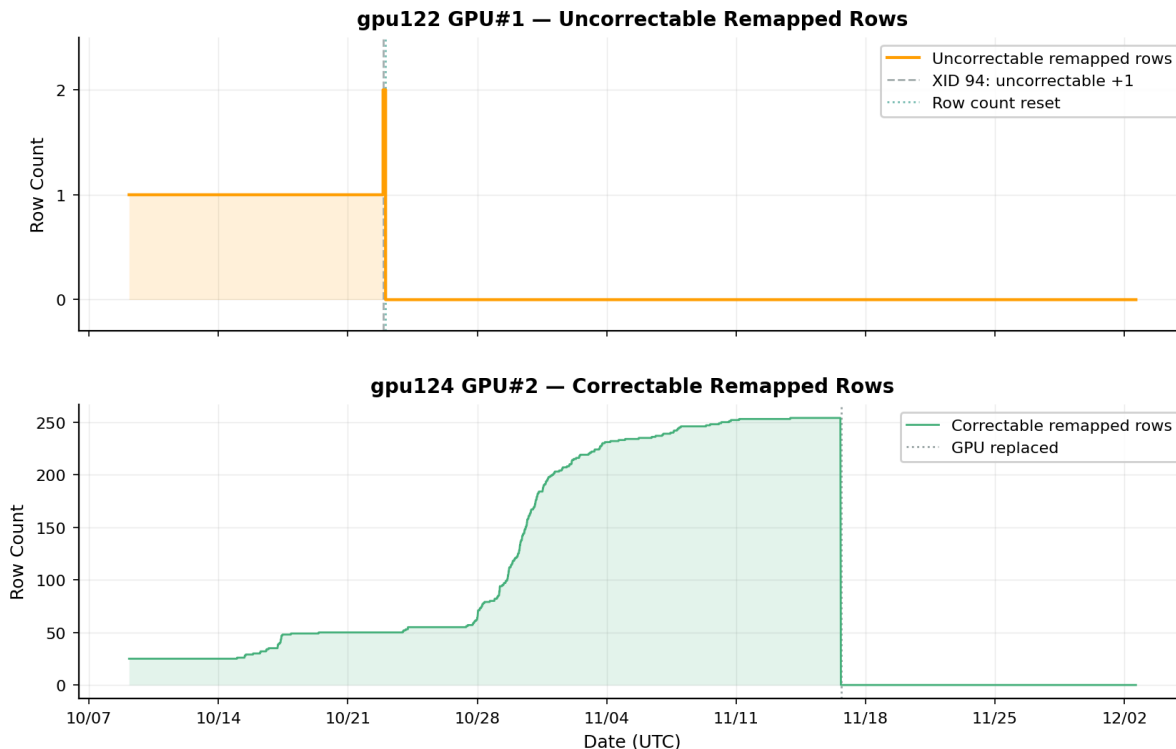


Figure 4: ECC memory row remapping timeline. Top — gpu122 GPU#1 uncorrectable (permanent fault) remapping: when remappings increased, XID 94 ECC error fired simultaneously, halting the GPU. Bottom — gpu124 GPU#2 correctable (hardware auto-corrected) remapping: accumulated up to 254 rows over 55 days at an accelerating pace, with no XID error reported. The GPU was replaced on 11/17 because it was no longer visible to the system.

Across the 10 analyzed cases, no single precursor metric dominates consistently across failure types. Even within the same XID category (for example, NVLink 145/149) and even across recurrences on the same node (the two NVLink events on gpu071), the strongest signals differ. We therefore adopt a multi-signal strategy rather than relying on a single metric. Statistical detection over these 10 cases yields a 10/10 detection rate, 2/10 pre-XID detection (20%), and approximately 0.84 false positives per day. This result establishes a usable statistical baseline, but the low pre-XID rate and remaining false positives motivate follow-on ML modeling of multivariate time-series structure and cross-metric correlation changes.

4.2 Checkpoint Save and Recovery: Storage Bottleneck Analysis

Checkpoint behavior determines both the progress lost at failure time and the time required to resume training.

This section first characterizes the training I/O profile and checkpoint interval, then quantifies failure-induced loss and restart bottlenecks using W&B runs. It finally traces the checkpoint path from GPU VRAM to the NFS server using Prometheus metrics, which allows us to observe the asynchronous checkpoint pipeline and isolate the NFS RPC bottleneck.

4.2.1 Training I/O Profile and Checkpoint Interval

The time series can be partitioned into three training phases based on GPU utilization and NFS I/O patterns (Figure 5). In decreasing order of priority, we classify intervals as Save (checkpoint save; cluster-aggregate NFS writes > 20 GB/s), Load (checkpoint and data load;

GPU utilization $< 50\%$ and cluster-aggregate NFS reads > 2 GB/s), and Training (all remaining intervals).

During stable training, GPU utilization is maintained above 99%, with brief dips observed at approximately 2-hour 13-minute intervals. These dips are precisely synchronized with NFS write spikes, showing that checkpoint saves temporarily pause GPU computation. The per-node write volume per checkpoint is approximately 20 GB, remaining constant throughout the period; the cluster-aggregate peak write rate decreased from approximately 43 GB/s early in the analysis to approximately 31 GB/s after mid-November. The decrease in cluster-aggregate rate while per-node write volume remained constant suggests that the same amount of data was distributed over a longer duration. The precise cause (NFS server-side load, performance changes due to growing storage capacity, etc.) requires further investigation.

At session startup, NFS reads surge to approximately 230 GB/s cluster-aggregate due to checkpoint and training data loading, with approximately 200 GB loaded into the page cache per node over about 25 minutes. After this, NFS network traffic converges to virtually 0 during training, with all data access served from the page cache.

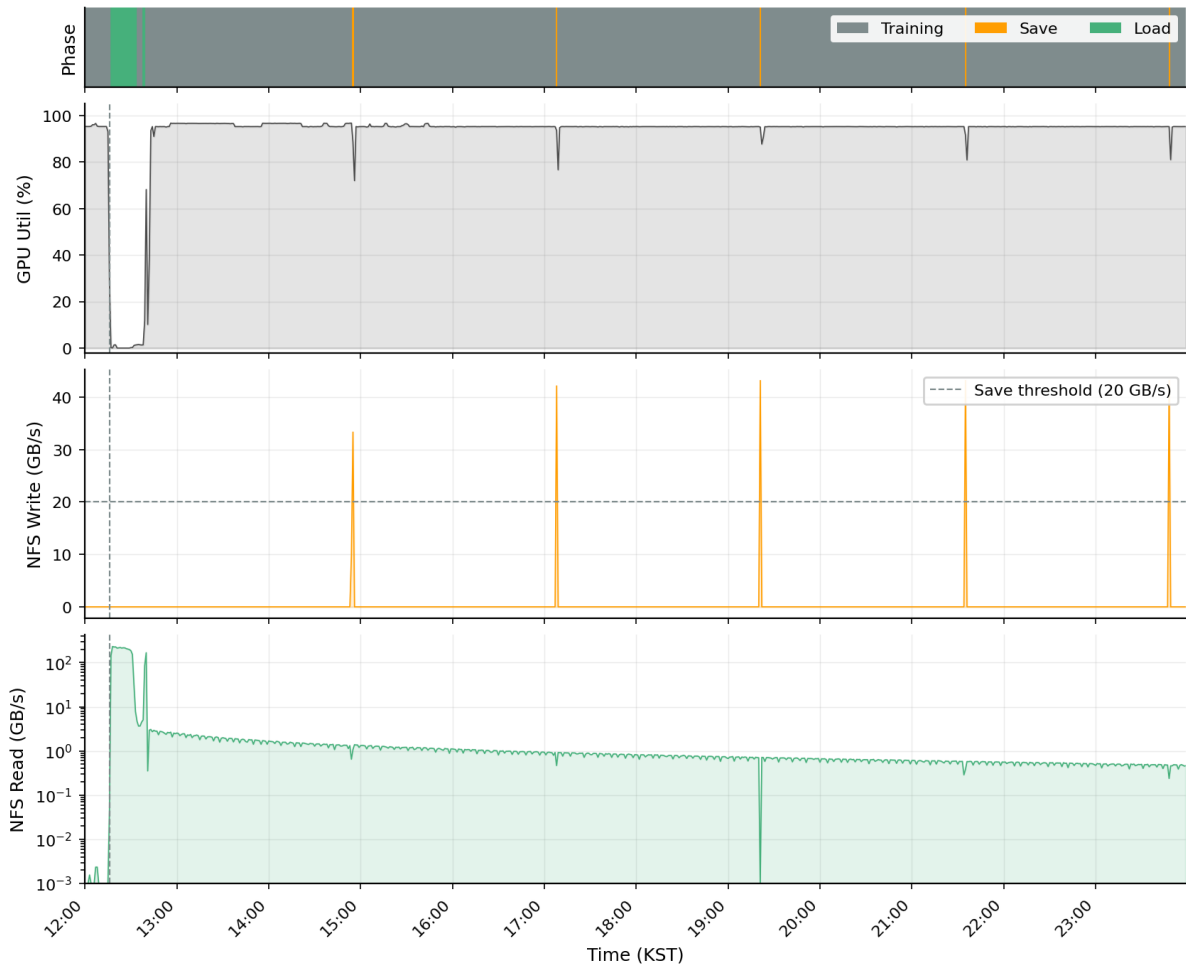


Figure 5: Training I/O profile (2025-10-25 12:00–10-26 00:00 KST). From top: training phase classification bar (gray=Training, orange=Save, green=Load), cluster-average GPU utilization (%), cluster-aggregate NFS write rate (GB/s, gray dashed line=20 GB/s Save detection threshold), cluster-aggregate NFS read rate (GB/s, log scale). Gray dashed line indicates session start time (12:16 KST).

A total of 523 checkpoint events were automatically detected over 55 days based on NFS write spikes. Checkpoints are stored on VAST Data NFS storage, and the interval varied

systematically with the training configuration. According to the Solar Open technical report [3](Section 3.4), training proceeds in three phases: pretraining (sequence length 4K, per-GPU batch 28, global batch 13,440), context extension phase 1 (32K, per-GPU batch 3, global batch 1,440), and context extension phase 2 (100K, per-GPU batch 1, global batch 480). The measured checkpoint intervals for each phase are as follows.

- **4K sequence phase** (pretraining): median 2.23 hours (133.5 min), standard deviation 5.4 min, stable. This phase accounted for most of the analysis period (466 events).
- **32K sequence phase** (context extension phase 1): increased to 3.32 hours (199 min), attributed to longer step times from the extended sequence length.
- **100K sequence phase** (context extension phase 2): 1.36 hours (81.5 min), shorter than 32K and close to the theoretical optimum; the optimization effect is discussed below.

NFS storage usage increased from approximately 450 TB to 963 TB during the analysis period, an increase of approximately 510 TB (Figure 6). Utilization changed from approximately 20% to 43% out of the total capacity of approximately 2,252 TB.

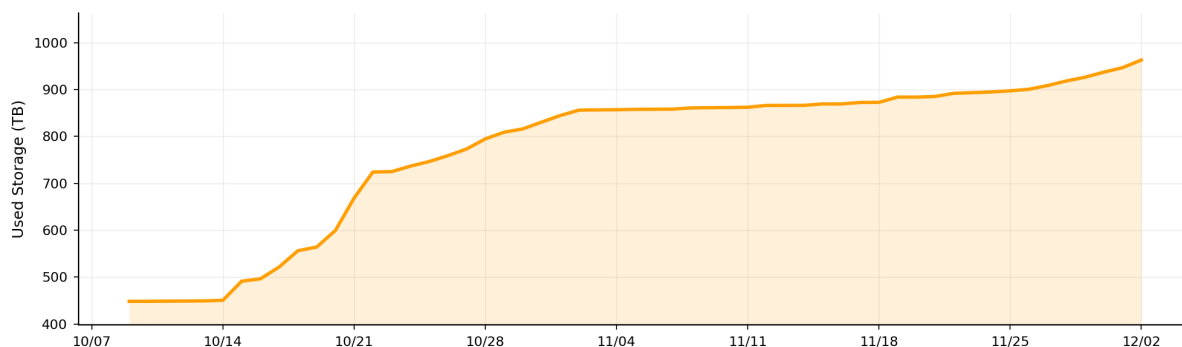


Figure 6: NFS storage usage trend over 55 days (total capacity approximately 2,252 TB). Checkpoint file accumulation is the primary driver of growth.

4.2.2 Failure Cost and Checkpoint Interval

Checkpoint interval sets a direct trade-off between save overhead and lost progress at failure time. More frequent checkpoints reduce lost work but increase save overhead, whereas longer intervals reduce overhead but increase the amount of discarded training. The Young/Daly model [19, 20] provides the standard reference point for this trade-off.

This model assumes that failures occur uniformly (memorylessly) over time. In practice, however, the lost-time distribution is not uniform: operator-initiated terminations shortly after checkpoints (loss 0.05–0.1 hours) coexist with unexpected failures in the mid-to-late interval (loss 2–3 hours) [21], so the theoretical optima below serve as reference points for setting operational targets. Nonetheless, an operational lesson can be drawn from this analysis: checkpoint save overhead ($\delta = 18\text{--}31.7$ seconds) is small enough that the cost of shorter intervals is low, and reducing the interval to 81.5 minutes in the 100K sequence phase brought total cost (1.82%) close to the theoretical optimum (1.72%).

Measured lost time. For 23 abnormally terminated W&B runs³, we identified the preceding checkpoint from NFS write spike timestamps and calculated the difference from the termination time (Figure 7). The mean lost time was 0.98 hours, with a total of approximately 22.6 hours.

³These 23 cases are abnormally terminated runs recorded in W&B, which differ in counting unit from the 17 events in Table 2 (Prometheus/XID-based failure events): W&B runs represent session terminations from the training framework perspective, while Table 2 counts hardware-layer XID error occurrences.

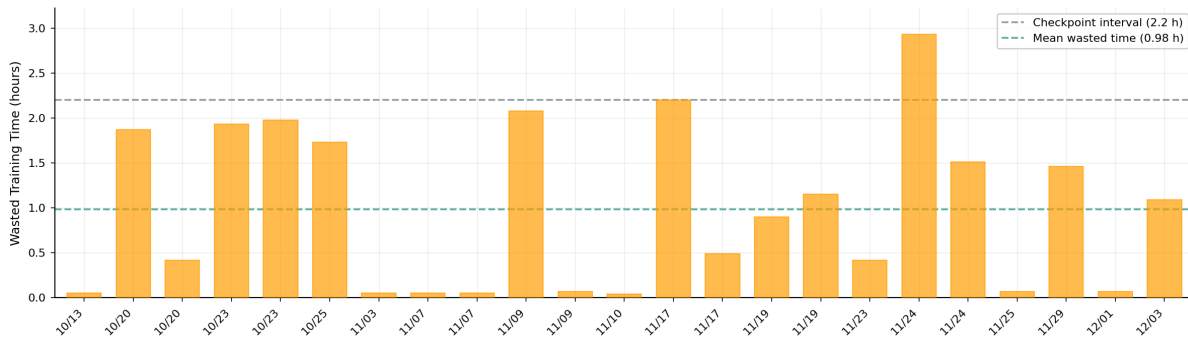


Figure 7: Lost training time per abnormally terminated W&B run (23 cases). Gray dashed line = 4K-stage checkpoint interval (2.2 hours), teal dashed line = mean lost time (0.98 hours).

Interval optimization. Checkpoint intervals involve a trade-off: shorter intervals increase save overhead (δ/T), while longer intervals increase the average loss upon failure ($T/2M$). The Young/Daly model gives the optimal interval $T_{\text{opt}} = \sqrt{2\delta M}$.

Save duration δ cannot be measured directly at 30-second Prometheus sampling, so we estimated it from the number of consecutive NFS write spike samples (Table 10). MTBF (M) was estimated at 56.2 hours from 1,294 total training hours across 24 runs divided by 23 abnormal terminations.

Table 10: Statistical estimation of checkpoint save duration (δ). \bar{N} is the average number of consecutive 30-second samples spanned by an NFS write spike.

Training Phase	Episodes	\bar{N} (samples)	δ (sec)
4K sequence	466	1.60	18.0
32K sequence	36	2.06	31.7
100K sequence	21	2.00	30.0

Table 11 compares costs by training phase. In the 4K and 32K phases, the actual interval was approximately $3\times$ the theoretical optimum, with failure loss (1.98–2.95%) dominating the cost. In the 100K phase, the interval was shortened to 81.5 minutes ($1.4\times$ the optimum), and total cost (1.82%) was within 0.10 percentage points of the theoretical minimum (1.72%). Save overhead remained below 0.6% in all phases, confirming the low cost of shorter intervals.

Table 11: Checkpoint interval cost comparison by training phase ($M = 56.2$ hours).

Training Phase	δ	Actual Interval	T_{opt}	Save Overhead	Total Cost
4K sequence	18 s	133.5 min	44.9 min	0.22%	2.20%
32K sequence	31.7 s	199.0 min	59.7 min	0.27%	3.22%
100K sequence	30 s	81.5 min	58.1 min	0.61%	1.82%

4.2.3 Restart Loading Time and Bandwidth Utilization

Restart loading time is a first-order determinant of recovery latency (Figure 8). We measured the time required to load checkpoints and datasets at session startup across 20 sessions that lasted more than 1 hour and for which the loading phase could be identified. Loading time is defined as the interval from session start to the end of the Startup/Loading phase (Section 4.2.1: GPU utilization $< 50\%$ and cluster-aggregate NFS reads > 2 GB/s). The mean loading time is 33 minutes and the median is 31 minutes. Variance is largely attributable to failure type (single-node replacement versus full-cluster reboot) and the availability of residual page cache.

Comparing the NFS read rate during each loading phase against the theoretical maximum bandwidth ($60 \text{ nodes} \times 25 \text{ GB/s} = 1,500 \text{ GB/s}$), the average utilization is approximately 10%. At one-tenth of the theoretical bandwidth, a network upgrade ($200 \text{ Gbps} \rightarrow 400 \text{ Gbps RoCE}$) would not reduce restart time. The actual location of the bottleneck is identified in Section 4.2.5.

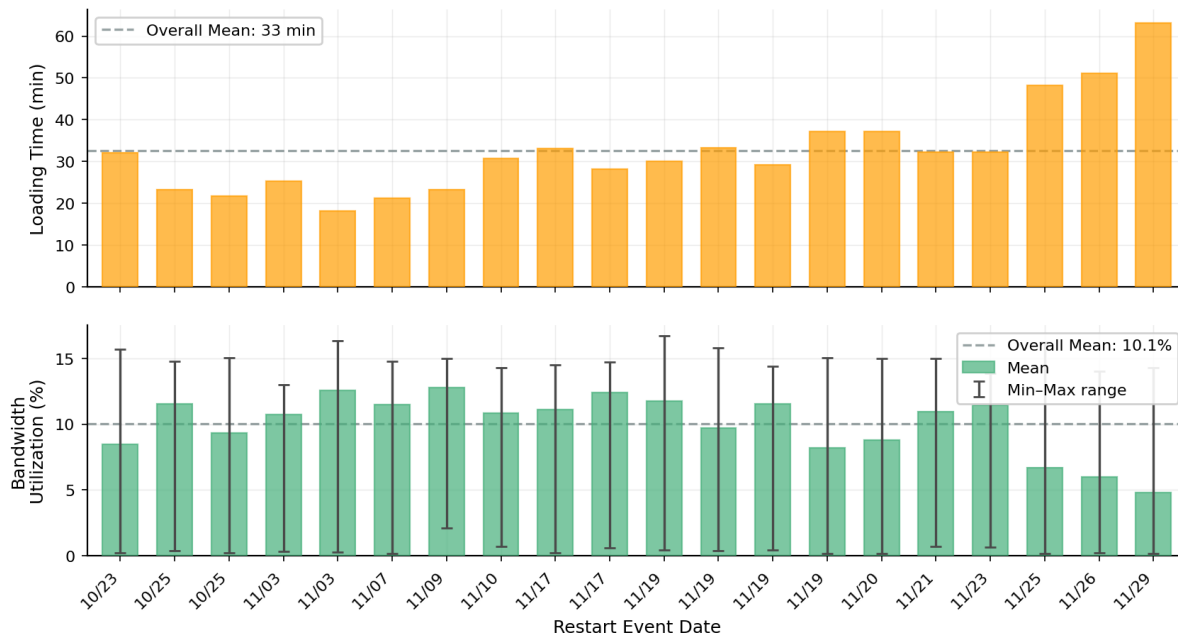


Figure 8: Session loading time and NFS bandwidth utilization (20 sessions). Top: loading time (minutes), gray dashed line = mean (33 min). Bottom: NFS read utilization relative to theoretical maximum bandwidth (1,500 GB/s). Bars = mean, error bars = min to max (based on 30-second Prometheus sampling, overall mean 10.1%), gray dashed line = mean (10%).

Table 12 summarizes the key metrics from this section.

Table 12: Checkpoint I/O quantitative analysis summary (55 days, 60-node training on 63-node B200 cluster)

Category	Metric	Measured Value
Storage Usage	Start / End	450 TB / 963 TB
	Utilization Change	approx. 20% \rightarrow 43%
Checkpoints	Detected Events	523
	Interval (4K / 32K / 100K)	2.23 / 3.32 / 1.36 h
	Save Duration δ (4K / 32K / 100K)	18.0 / 31.7 / 30.0 s
	Per-node Write Volume	approx. 20 GB
	Cluster-aggregate Peak Write (30s avg)	31–43 GB/s
Failure Cost (23 runs)	Mean Lost Time	0.98 h
	Total Lost Time	22.6 h
Session Loading (20 sessions)	Loading Time Mean / Median	33 min / 31 min
	Mean Bandwidth Utilization	approx. 10%

4.2.4 Checkpoint Data Path: From GPU to NFS

Save path. Checkpoint saving operates as a two-phase asynchronous mechanism (Figure 9, left). In Phase 1 (blocking), the model/optimizer state in GPU VRAM is copied to a CPU-side staging buffer—a region pre-allocated in `/dev/shm` tmpfs in this cluster—pausing training.

In Phase 2 (asynchronous), the staging data is passed to the kernel page cache via `write()` system calls, after which writeback threads transmit it to the server via NFS WRITE RPCs while training resumes immediately. Although the two phases vary nearly simultaneously at 30-second sampling, the cascade order is consistently captured: GPU utilization drop → `/dev/shm` occupancy → `write()` → Dirty Pages → Writeback → IP Out / NFS Write → RPC backlog (128 slot saturation) → VAST storage growth.

`/dev/shm` usage stays constant once the staging buffer is pre-allocated at training start and the same region is reused for each save. The 60 training nodes split into two groups (48 nodes at approximately 48 GB, 12 nodes at approximately 9 GB), and the per-node NFS write volume per checkpoint follows the same split (approximately 26 GB and 2 GB, respectively); the larger `/dev/shm` region thus serves as the staging buffer for nodes that transmit their own shards directly to NFS. The cumulative `write()` system call volume and the NFS server received volume match exactly at 20.55 GB per node and 1,295 GB cluster-aggregate, confirming that all saved data passed through the `write()` path.

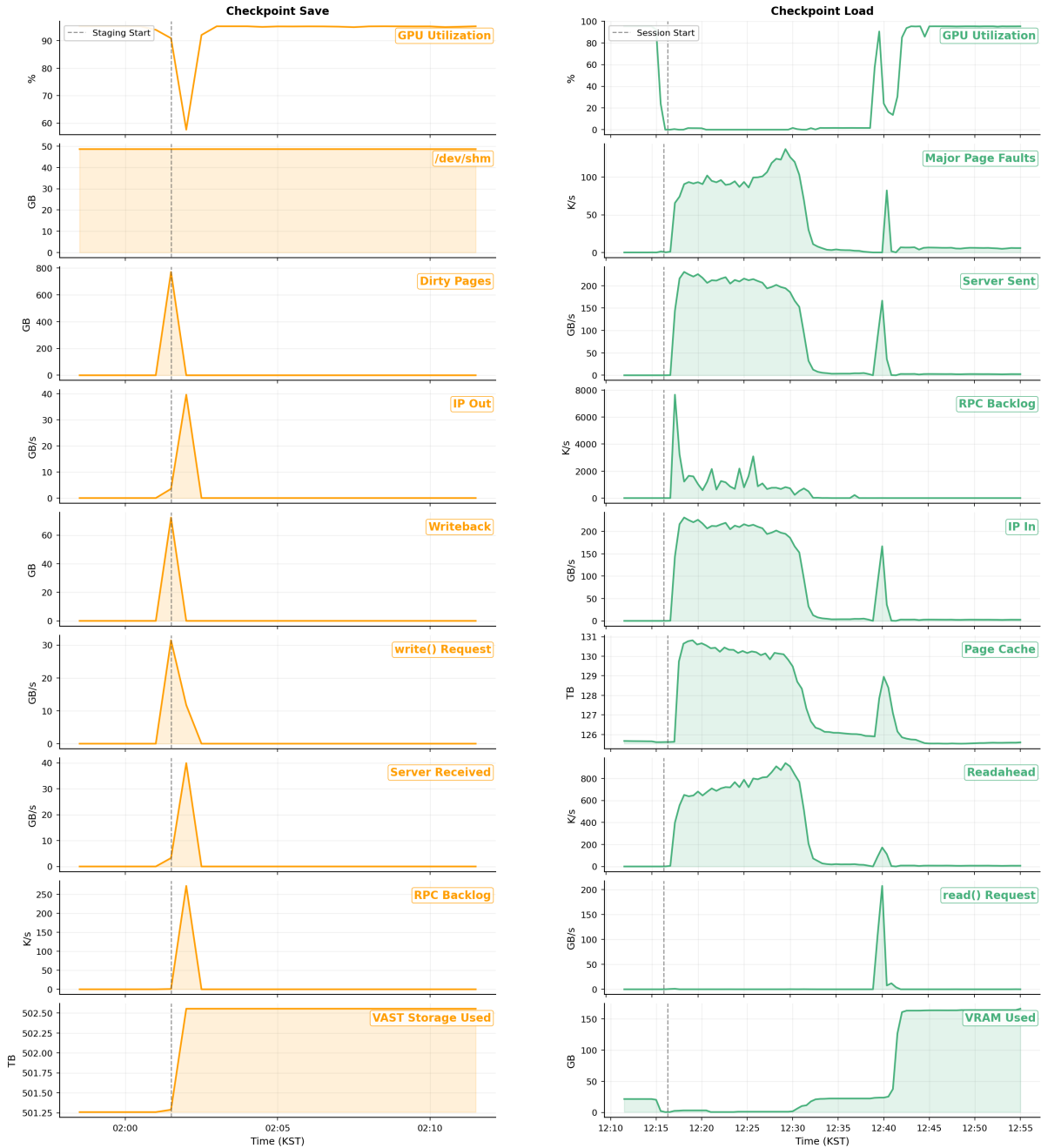


Figure 9: Checkpoint I/O data path profile. The left panel shows the save path and the right panel shows the load path, each laid out across 9 layer-level metrics in data-flow order. Dashed lines indicate staging start (left) and session start (right).

Load path. Checkpoint loading proceeds in two phases (Figure 9, right). In Phase 1 (`mmap` path, 0–22 minutes), the training framework maps checkpoint files into its memory address space via `mmap()`; major page faults on access trigger NFS READ RPCs, moving data from the NFS server into the kernel page cache. In Phase 2 (`read()` path, 22–28 minutes), `read()` system calls copy data from the page cache into user buffers, and the training framework then transfers data from user buffers to GPU VRAM via separate `cudaMemcpy` calls. The two phases are observed with a time gap spanning more than 30 minutes.

In Phase 1, NFS Read peaks at approximately 230 GB/s within 1–3 minutes of start, and the RPC backlog spikes (128 slot saturation). During this period, approximately 5 TB is loaded into

the page cache, while `read()` system calls remain almost negligible across the entire interval (cumulatively 1.5 GB per node, less than 0.1% of NFS Read). In Phase 2, `read()` surges within a single 30-second window at minute 24, copying 130–140 GB per node into user buffers. The cumulative `read()` of 162 GB during 22–28 minutes exceeds the same-interval NFS Read increase of 141 GB/node by 21 GB, the difference corresponding to data loaded into the page cache during Phase 1 that was served as cache hits. At minute 26, VRAM fills from 25 GB to 163 GB in a single step, with GPU utilization simultaneously rising from 0% to 94%, and VRAM loading completes at minute 40 (approximately 166 GB per GPU).

This cache hit matches the case where the previous session’s page cache persists across normal restarts. Because each node has ample RAM headroom (MemAvailable approximately 95%) on this cluster, cache persistence is possible, which we estimate as one factor behind the loading time variation reported in Section 4.2.3.

4.2.5 NFS RPC Bottleneck: Resolving the Bandwidth Paradox

The key question in restart loading is why the system uses only about 10% of the available 200 Gbps RoCE bandwidth. To answer it, we decompose the lifecycle of each NFS RPC into two components: (1) RPC slot wait, the time the client spends waiting for one of the 128 RPC slots per connection, and (2) network+server processing, the time spent after a slot is acquired to transmit the request, process it at the server, and receive the response. Using Prometheus counter-based NFS metrics (`queue_time_seconds_total` / `response_time_seconds_total` / `requests_total`), we compute per-request latency for each component (Figure 10).

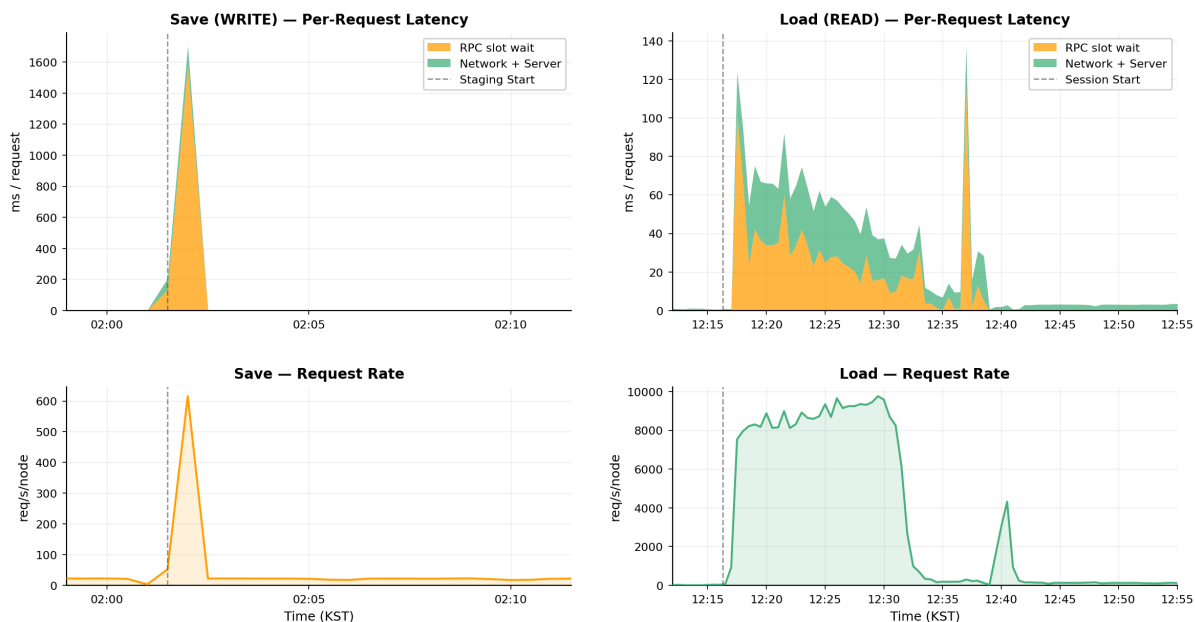


Figure 10: Per-request NFS RPC latency decomposition. Top: per-request latency decomposed into RPC slot wait (orange) and network+server processing (green). Bottom: per-node request rate. Save (WRITE) is concentrated in a single 30-second sample with a write spike, where per-request latency at that moment is approximately 1,621 ms. Load (READ) has low per-request latency (mean 59 ms; brief spikes of approximately 160 ms/req observed twice—about 1.5 minutes after start and around minute 24) but sustains a high request rate (8,000~9,000 req/s/node) for about 23 minutes.

Table 13: Comparison of RPC request patterns and per-request latency between save and load.

Measurement	Save (WRITE)	Load (READ)
Occurrence pattern	Concentrated in one 30-s sample	Sustained for ≈ 23 min
Per-node request rate	≈ 600 req/s (at peak)	Mean $\approx 5,400$, peak $\approx 9,000$ req/s
	Total	59 ms
Per-request latency	RPC slot wait	31.5 ms (53.3%)
	Network+server processing	27.3 ms (46.2%)

The measurements (Table 13) reveal two facts. First, during saves, RPC slot wait reaches 1.5 seconds, accounting for 92% of total latency. The bottleneck thus lies not in NFS server processing capacity or network bandwidth but in client-side RPC slot shortage. Second, since WRITE includes data payload transmission and durable storage (or commit) processing, the per-RPC server processing time is longer than for READ (126 ms vs. 27 ms). Within the same 128-slot limit, the number of requests processable per unit time is smaller, so write spikes during saves immediately saturate the slot queue.

Bandwidth paradox. The theoretical network bandwidth is 25 GB/s per node (200 Gbps RoCE), or 1,500 GB/s cluster-aggregate. At 30-second sampling, bandwidth utilization averages 1.4% (peak 2.7%) during saves and 10.4% (peak 14.7%) during loads. Upgrading from 200 Gbps to 400 Gbps would not shorten loading time, because the bottleneck lies not in the network bandwidth but in the RPC protocol layer above it (128-slot limit). Improvement directions include increasing the NFS client’s RPC slot limit, client-side I/O merging (readahead optimization), or reducing server-side response time.

4.3 Failure Patterns and Automated Recovery

This subsection analyzes failure response in multi-node training from two complementary perspectives. Section 4.3.1 asks *where* failures recur by identifying which nodes are repeatedly excluded and why. Section 4.3.2 asks *how effectively* the system recovers once a failure occurs. The two analyses are linked: the spare-node shortage that limits auto-retry effectiveness (Section 4.3.5) follows directly from the exclusion distribution.

4.3.1 Node Exclusion Patterns

Node exclusion is highly concentrated rather than uniformly distributed across the cluster. Across 224 multi-node training sessions over 73 days, the same nodes were repeatedly withheld from 60-node jobs. The cluster contains 63 GPU nodes. When a 60-node session starts, Sokovan selects from the set of nodes whose resources are currently free. Operators can deliberately exclude nodes from multi-node scheduling by pre-allocating single-node sessions to them. Because the cluster has only 3 spare nodes, and those spares are often occupied in this way, the effective node composition of large training jobs becomes nearly fixed.

Figure 11 shows the node exclusion distribution across 224 multi-node training sessions. The distribution is concentrated: the top 3 most-excluded nodes (gpu074, gpu119, gpu086) account for over 50% of all exclusions, while most nodes have exclusion rates below 5%.

Of the 73-day analysis period (1,403 hours), 60-node training sessions ran for 1,356 hours, representing a temporal occupancy of 96.6%. The longest session ran for 222.9 hours (9.3 days), and the top 5 sessions each ran continuously for more than 3.6 days.

To analyze the causes of node exclusion, we computed the fraction of 60-node-training exclusion time that overlaps with single-node session allocation on the same node (Figure 12, 13). This ratio serves as an indicator distinguishing whether a node was deliberately isolated by an operator (single-node session occupancy) or naturally not selected as a consequence of the scheduler choosing 60 out of 63 nodes.

Many of the top-excluded nodes correspond to deliberate isolation. For gpu074 (100%), gpu086 (97%), gpu116 (99.6%), and gpu113 (92%), nearly all the exclusion time overlaps with single-node occupancy, the result of operators explicitly isolating these nodes by assigning single-node sessions out of concern for performance degradation (communication delays, reduced training speed, etc.). gpu119 (69%, with absolute overlap of 793 hours) and gpu122 (72%, 447 hours) show somewhat lower ratios, but their absolute overlap times are substantial, classifying them as nodes frequently subject to deliberate isolation.

In contrast, gpu085 (4% of 393 excluded hours) and gpu098 (2% of 20 excluded hours) barely overlap with single-node occupancy, suggesting they were not deliberately isolated but naturally not selected as a consequence of the scheduler choosing 60 out of 63 nodes.

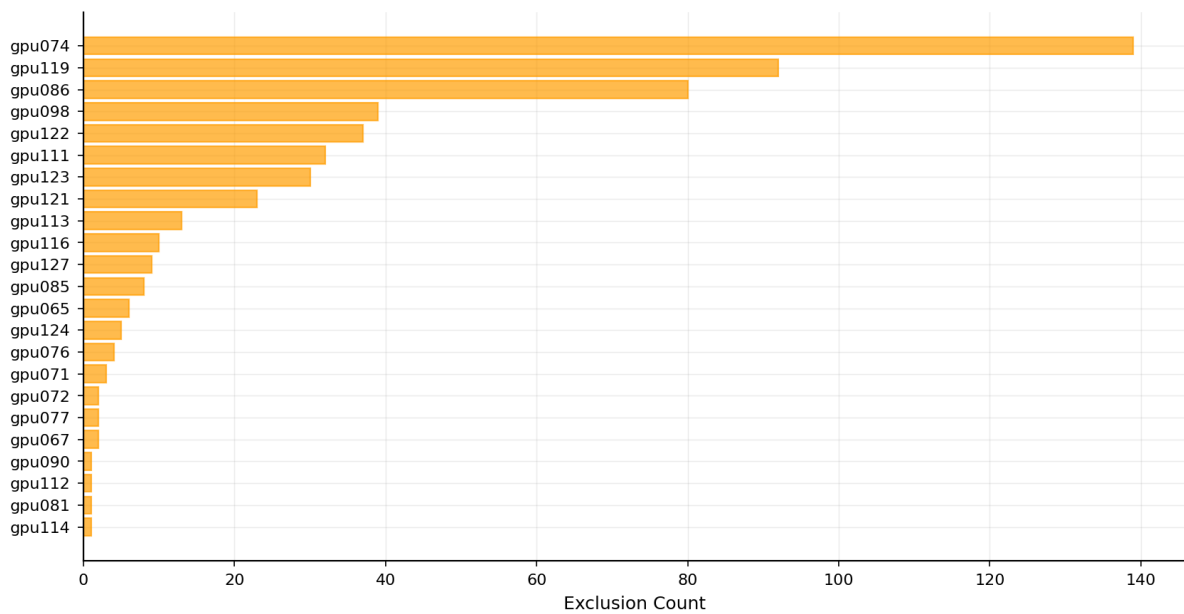


Figure 11: Node exclusion frequency across 224 multi-node training sessions over 73 days. The top 3 nodes (gpu074, gpu119, gpu086) account for over 50% of all exclusions, showing a concentrated distribution.

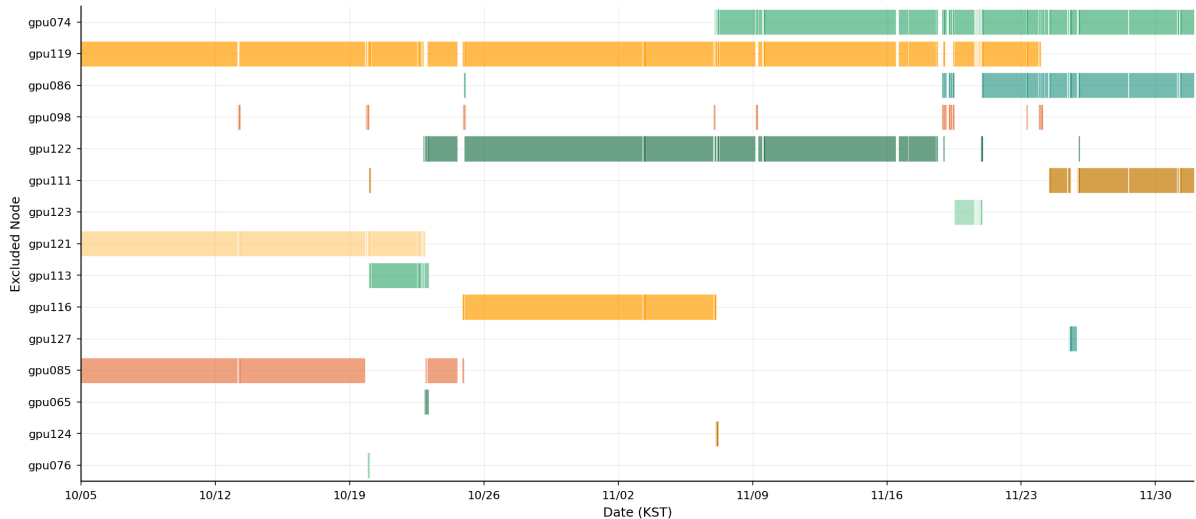


Figure 12: 60-node training session exclusion timeline for the top 15 nodes. Each bar represents the duration during which the node was excluded from a training session. Compared with Figure 13, most exclusions overlap temporally with deliberate single-node occupancy.

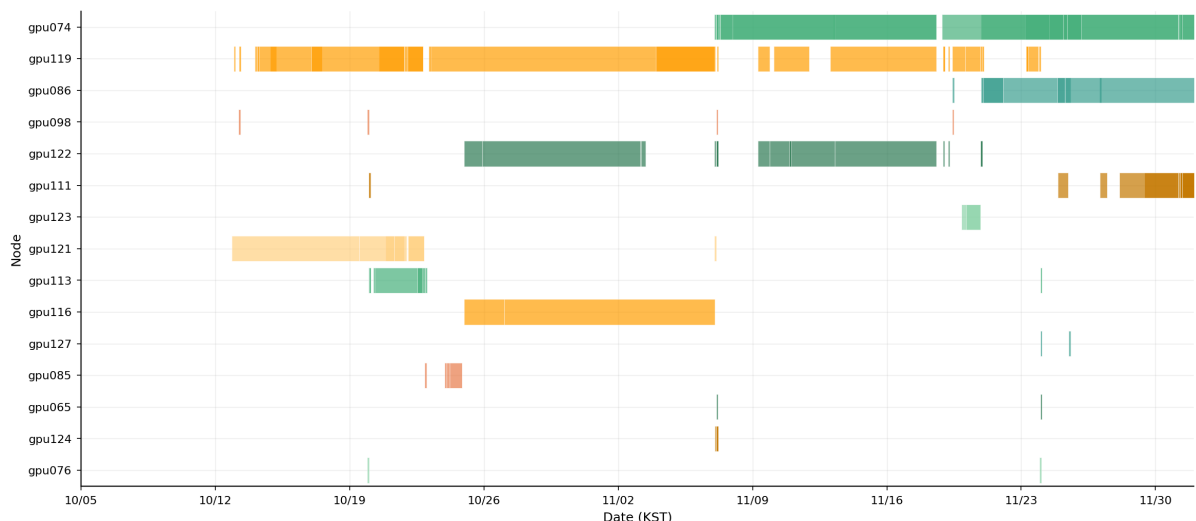


Figure 13: Single-node session occupancy timeline for the same 15 nodes. The pattern shows operators allocating single-node sessions to problem nodes to deliberately exclude them from 60-node training scheduling. For gpu074 (100%), gpu086 (97%), and gpu116 (99.6%), nearly all of the 60-node-training exclusion time overlaps with single-node occupancy.

In summary, the top 3 nodes (gpu074, gpu119, gpu086) account for over 50% of all exclusions in a concentrated distribution, and many of these correspond to operators’ deliberate exclusion (explicit isolation via single-node session occupancy). Some nodes (such as gpu085) do not overlap with single-node occupancy and appear to have been naturally excluded as a consequence of the scheduler’s random non-selection.

4.3.2 Auto-Retry Chain Analysis

The auto-retry analysis evaluates how quickly and how reliably recovery proceeds after failure. Backend.AI FastTrack exposes auto-retry controls at the task level (Figure 14) through three parameters: whether retry is enabled, the maximum retry count, and the retry delay. During

the observation period, retry was enabled and the delay was set to approximately 10 minutes. The following results quantify the operational effect of that configuration.

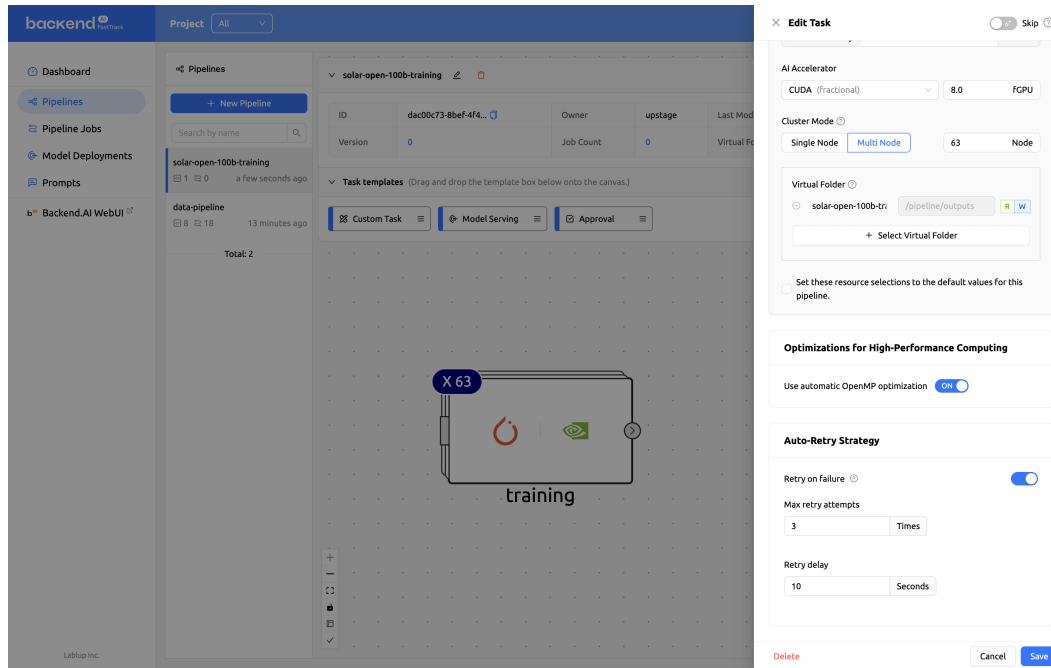


Figure 14: Backend.AI FastTrack auto-retry configuration screen. Operators can configure per-task settings for retry on failure, maximum retry count, and retry delay. Additional options include resource configurations such as GPU count, node count, and storage mounts.

From 73 days of operational logs, sessions consecutively executed under the same task name were grouped as auto-retry “chains.” Twelve such chains (73 attempts in total, 61 retries) were identified, with results shown in Table 14.

Table 14: Result classification of 12 auto-retry chains.

Result	Description	Count
SUCCESS	Training reached after retry	4
FAIL (after training)	First attempt reached training, all subsequent retries failed	3
FAIL (start failure)	Failed from the start, all retries failed	5

Figure 15 shows the chronological timeline of all sessions.

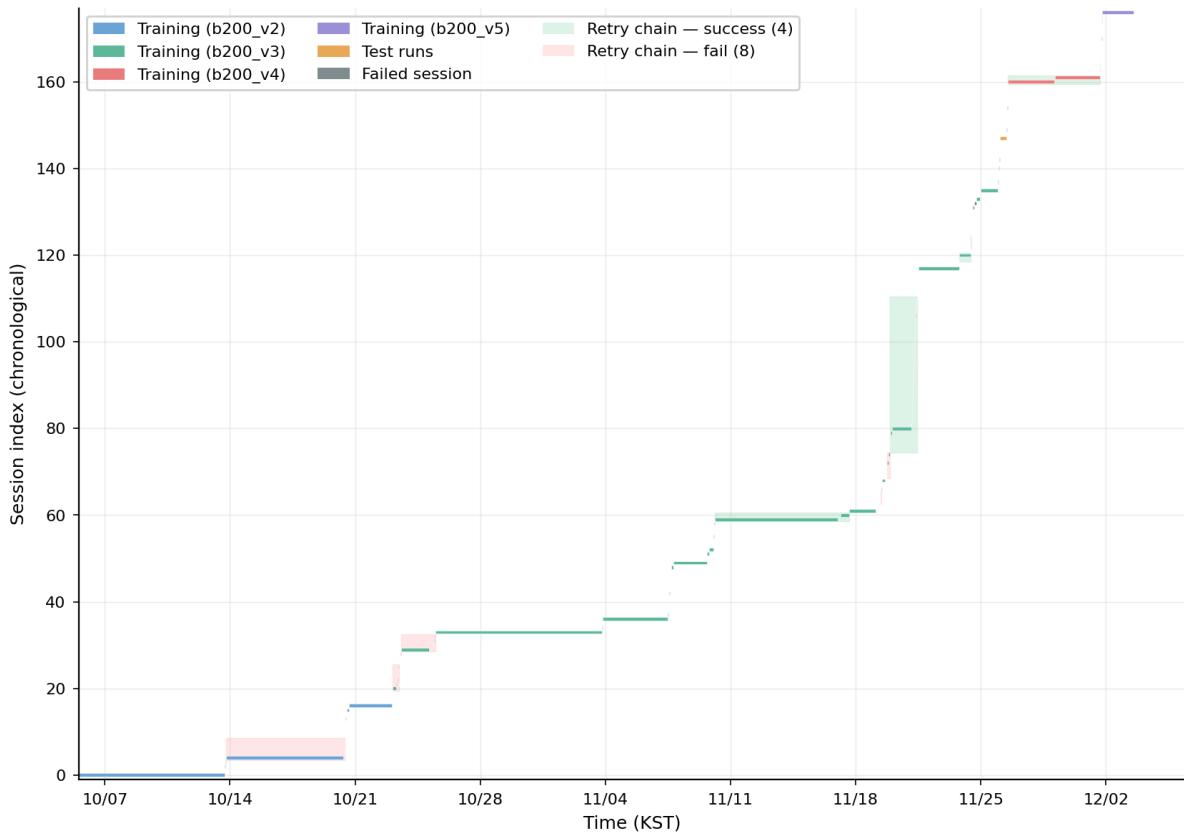


Figure 15: 73-day session timeline. The x-axis is time; the y-axis is the order of session start times. Each bar represents a single 60-node session, and colors distinguish training versions (b200_v2–v5). Background highlights indicate auto-retry chains: green for chains that successfully resumed training after retries (4), pink for chains that failed (8).

4.3.3 Retry Interval Predictability

FastTrack’s configured retry delay produces a highly regular restart cadence (Figure 16). Auto-retry inter-session gaps have a median of 11 minutes with IQR 10–11 minutes, which matches the 10-minute retry delay plus teardown and restart overhead. Manual restarts have a shorter median of 2 minutes but a far wider range of 0–430 minutes, making them operationally unpredictable. The contrast is especially important at night and on weekends, when human response may be delayed but auto-retry continues to act on a fixed schedule.

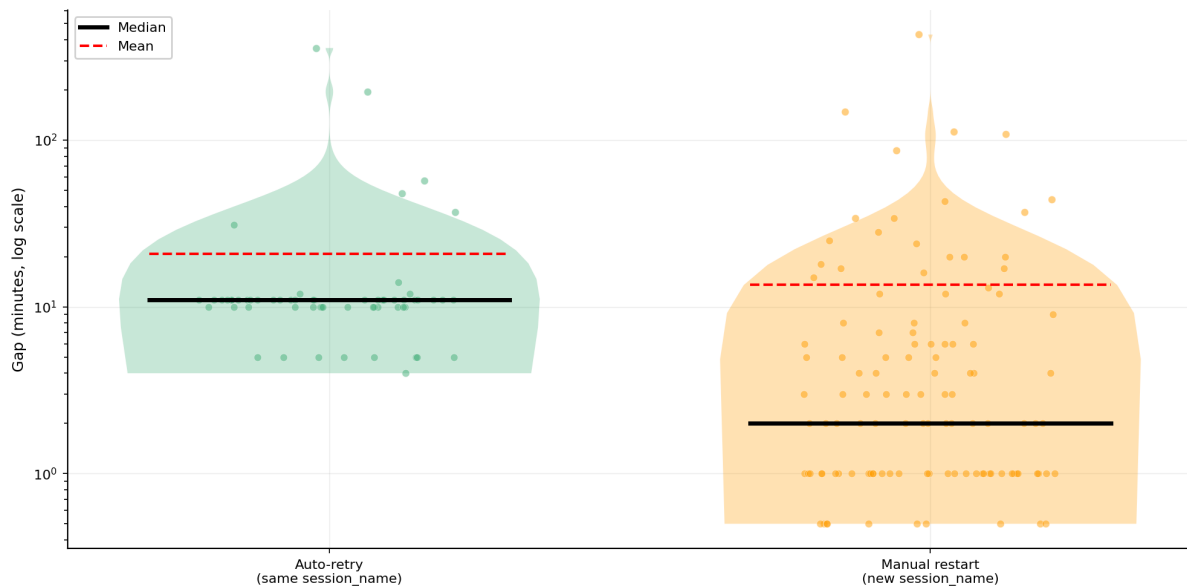


Figure 16: Comparison of inter-session gap distributions between auto-retry and manual restart. Auto-retry has median 11 minutes, IQR 10–11 minutes, corresponding to the FastTrack retry delay setting. Manual restart has median 2 minutes but a range of 0–430 minutes, unpredictable depending on response timing.

4.3.4 Success Rate Comparison and Downtime Reduction

Auto-retry improves recovery success for transient failures, although its benefits are bounded by the structure of the underlying failure. The chain success rate—the fraction of retry sequences under the same task name that reached training at least once—was 33.3% (4 of 12 chains). By comparison, only 12.5% of manually started individual sessions (13 of 104) reached training, making the chain success rate approximately $2.7\times$ higher. Chains are naturally advantaged because they include multiple attempts, but the gap still reflects the structural value of automated retries. Three of the 4 successful chains recovered after a single retry. One of them involved XID 94 (ECC error), which Table 3 classifies as `RESTART_APP`; this case shows that auto-retry can restore progress without operator intervention.

This improvement in success rate translates directly to downtime reduction. Analyzing 21 recovery episodes across 22 training sessions (Figure 17), the 4 episodes where auto-retry restored training had a median downtime of 1.9 hours, compared to 3.3 hours for 17 manual recovery episodes—a difference of approximately $1.8\times$. The large variance in manual recovery (0–53 hours) reflects cases where failures occurred during nighttime or weekends when immediate response was difficult.

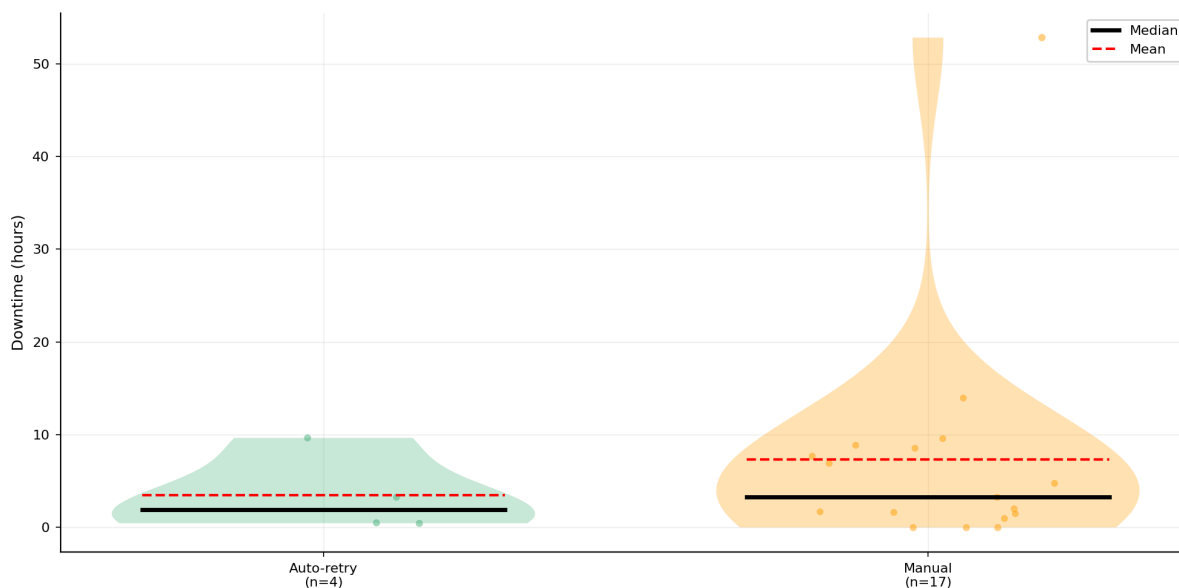


Figure 17: Downtime comparison between auto-retry and manual recovery (21 recovery episodes between training sessions). Auto-retry recoveries (green): median 1.9 hours. Manual recoveries (orange): median 3.3 hours. Black solid line = median, red dashed line = mean.

4.3.5 Structural Failures and Auto-Retry Limits

Most auto-retry failures were structural rather than transient. Eight of 12 chains (67%) ultimately failed, and most of these failures were caused by software- or network-level issues (for example, NCCL communication errors) that simple restarts could not resolve.

Additionally, auto-retry episodes with long downtimes (9.65 hours, 3.25 hours) were caused by infrastructure-level problems rather than limitations of the auto-retry mechanism itself. After hardware replacement, GPU licenses were not renewed, preventing nodes from joining the available resource pool, which caused retries to fail for hours as the 60-node requirement could not be met. This issue was subsequently resolved by switching to a floating license model.

The retry cost of failed chains was approximately 35 GPU-hours (2.7% of total training time). In particular, one chain failed 30 consecutive times after 25.4 hours of successful training, illustrating that repeated retries under the same conditions without resolving the underlying problem only consume GPU-hours.

This analysis suggests the following improvement directions:

- Exponential backoff: increasing retry intervals progressively (10 min \rightarrow 20 min \rightarrow 40 min) to reduce resource consumption in later retries while maintaining fast initial recovery for transient failures.
- XID-based branching: differentiating retry strategies by resolution type from Table 3. `RESTART_APP` types (XID 31, 43, 94) retry immediately; `RESET_GPU` types (XID 119, 145, 149) retry after GPU reset; `CONTACT_SUPPORT` types (XID 79) halt retries and notify operators.
- Priority-based session preemption: with only 3 spare nodes (Section 4.3.1), if single-node sessions occupy them, 60-node gang scheduling cannot meet its requirements and auto-retry can be delayed. Granting higher priority to multi-node training and automatically preempting lower-priority single-node sessions during retries, or expanding the spare node pool, could improve availability.

5 Limitations

This report evaluates infrastructure-level recovery behavior rather than end-to-end training efficiency. The checkpoint I/O analysis in Section 4.2 partly addresses this gap by quantifying checkpoint overhead ($\delta = 18\text{--}31.7$ seconds), lost time per failure (mean 0.98 hours), restart loading time (mean 33 minutes), and the RPC bottleneck mechanism. However, measuring how those effects translate into overall training efficiency requires instrumentation inside the training framework, which lies outside the present scope.

The precursor analysis in Section 4.1 is also retrospective. Real-time deployment would require separate validation of the false-positive distribution and the operational burden imposed by alerts. The 10 analyzed failure cases further limit statistical power.

Finally, the auto-retry analysis covers only 12 chains (73 attempts). The results are sufficient to reveal structural properties of recovery behavior, but they remain limited in sample size.

6 Related Work

GPU cluster scheduling. GPU cluster scheduling has progressed from attained-service-based priority (Tiresias [22]) and introspective time-slicing (Gandiva [23]) to goodput-adaptive systems such as Pollux [24] and Sia [25], and more recently to work on fairness [26], network topology [27], geo-distributed scheduling [28], and cloud resource management [29]. These systems typically optimize JCT or goodput through workload-adaptive control. By contrast, Sokovan emphasizes predictable scheduling latency through hint-based polling and does not currently perform per-workload adaptive optimization.

Distributed training systems. Distributed training research has focused primarily on parallelization strategy, including model parallelism (Megatron-LM [30, 31]), pipeline parallelism (GPipe [32]), memory-efficient sharding (DeepSpeed ZeRO [33], PyTorch FSDP [34]), automatic strategy selection (Alpa [35]), and 10,000+ GPU scaling (MegaScale [5]). Backend.AI operates at a different layer: it manages session lifecycle and resource allocation rather than parallelization itself.

Fault tolerance and checkpointing. Checkpoint-based recovery remains fundamental to long-running training. Prior work spans frequency optimization (CheckFreq [36]), predictive checkpointing [37], in-memory checkpoints (Gemini [38], ByteCheckpoint [39]), checkpoint-free resilience through pipeline templates (Oobleck [40]), and redundant computation (Bamboo [41]). End-to-end fault-tolerant systems include elastic spot-VM training (Varuna [42]), fast failure detection (TRANSOM [43]), and MoE-specific resilience (Lazarus [44]), the last of which targets the same architectural class as the workload studied here. These systems primarily optimize checkpointing behavior or fault tolerance within the training stack itself. Our auto-retry mechanism instead performs session restart and resource reallocation at the orchestration layer while delegating checkpoint creation and restoration to the training framework. Section 4.3.3 quantifies the resulting restart times.

7 Conclusion

This report analyzed failure precursor detection, checkpoint I/O behavior, and automated recovery on a 63-node B200 production GPU cluster using 55 days of monitoring data.

7.1 Summary of Key Findings

The three analyses in Section 4 yield four findings, which we distill below into four broader principles. All four depend on the cross-organizational operational setting described in Section 3.5: without a shared metric pipeline across organizational boundaries, the production-scale phenomena summarized here would not have been directly observable.

Failures are a structural characteristic of large-scale training. The mathematical relationship between cluster scale and failure frequency, along with operational evidence (419 interruptions over 54 days on 16K GPUs; concentrated node exclusion patterns on a 63-node cluster), confirms that hardware failures every few hours are a fundamental characteristic of large-scale training.

Training workloads require session-level abstraction. Container orchestration assumes stateless, short-lived processes. Training workloads are stateful and long-running, requiring an abstraction that tracks checkpoint progress and enables resumption rather than restart. Backend.AI’s session abstraction decouples training progress from container lifecycle (Section 3.2).

GPU scheduling and storage must be co-designed. CPU-centric resource models fail to capture GPU topology or all-or-nothing allocation requirements. The storage I/O bottleneck observed in our cross-organizational setting (Section 3.5) illustrates this: provisioning GPU capacity without matching storage bandwidth creates performance cliffs that manifest only at operational scale. Full-stack profiling of checkpoint I/O (Section 4.2.5) revealed that the cause of the “bandwidth paradox”—where only 1.4–10.4% of 200 Gbps RoCE bandwidth is used—lies in the saturation of 128 slots in the NFS RPC protocol layer, indicating that what is needed is not a network bandwidth upgrade (200 Gbps→400 Gbps) but rather increased RPC slot limits or reduced server-side response time. Sokovan provides the GPU-side solution through GPU-first allocation combined with gang scheduling.

Observability is the foundation for automation and prediction. Monitoring signals must be directly connected to the failure handling pipeline—first for reactive automation (failure detection and recovery triggering), then for proactive prediction (identifying degradation patterns before failures occur). Precursor analysis (Section 4.1) showed that multi-signal statistical detection achieved a 10/10 detection rate with approximately 0.84 false positives per day across the 10 cases, while the pre-XID detection rate was limited to 2/10. Because no single precursor metric is consistently distinctive across failure types, a multi-signal approach that evaluates many metrics simultaneously is essential, and time-series ML modeling is in progress as a follow-up to improve the pre-XID detection rate. Auto-retry chain analysis (Section 4.3.2) showed that automatic retries achieve a 2.7× higher recovery success rate than manual recovery for transient failures while mechanically failing for structural failures (node availability < 60), indicating that detection signals must be connected to recovery strategies.

7.2 Future Work

Several limitations of this study stem from missing instrumentation during the observation period. Future training campaigns should therefore add the following measurements.

Training efficiency metrics. The current analysis measures infrastructure-level figures (checkpoint intervals, restart times, failure rates) but lacks metrics internal to the training framework. Logging per-iteration throughput (tokens/sec) would enable MFU calculation

and direct quantification of how infrastructure events—failures, restarts, node replacements—impact effective training progress. This can be collected through a simple configuration change to the training framework logger before training begins.

RPC bottleneck optimization. Section 4.2.5 identified the restart loading bottleneck as lying in the NFS RPC protocol layer rather than in the network bandwidth. During saves, WRITE requests spend approximately 92% of their time waiting for an RPC slot (about 1,495 ms per request); during loads, READ requests sustain 8,000~9,000 req/s/node for about 23 minutes, with brief response-latency spikes of approximately 160 ms/req shortly after start and around the 24-minute mark. Increasing the NFS client RPC slot limit, reducing server-side response time, or introducing a dedicated high-throughput I/O path for checkpoints are directions for future improvement.

Precursor-based predictive failure management. The statistical multi-signal detection in Section 4.1 achieved a 10/10 detection rate, 2/10 (20%) pre-XID detection, and approximately 0.84 false positives per day across the 10 cases, but the low pre-XID detection rate is the principal limitation. In many failures on this cluster, signals do not deteriorate gradually but emerge abruptly at the XID time point, which makes pre-XID detection difficult. To address this, ML modeling that captures multivariate time-series patterns and changes in cross-metric correlations is in progress; for operational deployment, real-time inference must be validated against false positives and an integrated design that automatically reflects detection results in auto-retry decisions is additionally required.

Intelligent resource adjustment and log analysis. Future work includes exploring an automated operations design that combines automatic resource adjustment upon OOM [45], detection of resource over-allocation, and integrated analysis across heterogeneous logs.

FP8 and reduced-precision training. Reduced-precision formats such as FP8 and MXFP8 promise throughput improvements but introduce failure modes in both the software stack and numerical stability. NVIDIA cuDNN releases document numerous FP8-related defects [46], Fishman et al. [47] showed catastrophic instability after approximately 200 billion tokens, and Lee et al. [48] demonstrated the lack of general robustness in current FP8 methods. The Solar Open project adopted FP8 + bfloat16 mixed precision on the same B200 cluster [3]. From an infrastructure perspective, developing an automated failure attribution mechanism that distinguishes whether training divergence originates from cuDNN bugs, numerical limitations, or hardware defects remains an open challenge.

Acknowledgments

This work was conducted as part of the Sovereign AI Foundation Model Project (GPU Track), led by the Ministry of Science and ICT (MSIT) and supported by the National IT Industry Promotion Agency (NIPA) (PJT-25-080041).

The storage I/O debugging case study in Section 3.5 was made possible by collaboration across multiple organizations. We thank SKT for cloud infrastructure and operational support, NVIDIA Korea for hardware expertise and driver-level diagnostics, VAST Data for storage-system analysis and configuration optimization, and Upstage for sharing workload characteristics and participating in joint debugging sessions.

We also thank the open-source communities that provide the tools and frameworks on which Backend.AI is built, including PyTorch, NCCL, and the Linux kernel networking stack.

Data Availability

The operational data analyzed in this report—including Prometheus time-series metrics, node exclusion logs, auto-retry records, and GPU utilization traces—was collected from a production cluster operated under the Sovereign AI Foundation Model Project and contains proprietary workload information. These datasets cannot be released because of contractual and confidentiality constraints. The Backend.AI platform itself is available as open-source software at <https://github.com/lablup/backend.ai>. The `all-smi` monitoring tool is available at <https://github.com/lablup/all-smi>. Aggregate statistics sufficient to reproduce the analyses presented in this report are provided in the tables and figures within the main text.

References

- [1] Aaron Grattafiori, Abhimanyu Dubey, et al. The llama 3 herd of models. *arXiv preprint arXiv:2407.21783*, 2024.
- [2] Apostolos Kokolis, Michael Kuchnik, John Hoffman, Adithya Kumar, Parth Malani, Faye Ma, Zachary DeVito, Shubho Sengupta, Kalyan Saladi, and Carole-Jean Wu. Revisiting reliability in large-scale machine learning research clusters. In *Proceedings of the 2025 IEEE International Symposium on High-Performance Computer Architecture (HPCA)*. IEEE, 2025.
- [3] Upstage Solar Team. Solar open technical report. Technical report, Upstage, January 2026. arXiv:2601.07022. 102B bilingual MoE (12B active) trained on 20T tokens. Also available at <https://huggingface.co/upstage/Solar-Open-100B>.
- [4] Myeongjae Jeon, Shivaram Venkataraman, Amar Phanishayee, Junjie Qian, Wencong Xiao, and Fan Yang. Analysis of Large-Scale Multi-Tenant GPU clusters for DNN training workloads. In *2019 USENIX Annual Technical Conference (USENIX ATC 19)*, pages 947–960, Renton, WA, July 2019. USENIX Association.
- [5] Ziheng Jiang, Haibin Lin, Yinmin Zhong, Qi Huang, Yangrui Chen, Zhi Zhang, Yanghua Peng, Xiang Li, Cong Xie, Shibiao Nong, et al. Megascale: Scaling large language model training to more than 10,000 gpus. In *Proceedings of the 21st USENIX Symposium on Networked Systems Design and Implementation (NSDI)*. USENIX Association, 2024.
- [6] Alexander Erben and Ege Erdil. Hardware failures won’t limit AI scaling. Epoch AI, 2024.
- [7] Yangtao Deng, Xiang Shi, Zhuo Jiang, Xingjian Zhang, Lei Zhang, Zhang Zhang, Bo Li, Zuquan Song, Hang Zhu, Gaohong Liu, Fuliang Li, Shuguang Wang, Haibin Lin, Jianxi Ye, and Minlan Yu. Minder: Faulty machine detection for large-scale distributed model training. In *Proceedings of the 22nd USENIX Symposium on Networked Systems Design and Implementation (NSDI)*, pages 505–521. USENIX Association, 2025.
- [8] Tianyuan Wu, Wei Wang, Yinghao Yu, Siran Yang, Wenchao Yang, Qinkai Duan, Guodong Yang, Jiamang Wang, Lin Qu, and Liping Zhang. FALCON: Pinpointing and mitigating stragglers for large-scale hybrid-parallel training. *arXiv preprint arXiv:2410.12588*, 2024.
- [9] Jinkun Lin, Ziheng Jiang, Zuquan Song, Sida Zhao, Menghan Yu, Zhanghan Wang, Chenyuan Wang, Zuo Cheng Shi, Xiang Shi, Wei Jia, Zherui Liu, Shuguang Wang, Haibin Lin, Xin Liu, Aurojit Panda, and Jinyang Li. Understanding stragglers in large model training using what-if analysis. *arXiv preprint arXiv:2505.05713*, 2025.

- [10] NVIDIA Corporation. Analyzing XID errors — GPU deployment and management documentation. <https://docs.nvidia.com/deploy/xid-errors/analyzing-xid-catalog.html>, 2026. Accessed: 2026-02-15.
- [11] NVIDIA Corporation. NVIDIA Blackwell architecture technical brief: Powering the new era of generative AI and accelerated computing. Technical brief, NVIDIA Corporation, 2024. Version 1.1. Per Blackwell GPU: up to 192 GB HBM3e, up to 8 TB/s. Accessed: 2026-04-21.
- [12] NVIDIA Corporation. DGX SuperPOD: Next generation scalable infrastructure for AI leadership reference architecture featuring DGX B200. <https://docs.nvidia.com/dgx-superpod/reference-architecture-scalable-infrastructure-b200/latest/>, 2025. Document RA-11334-001. Accessed: 2026-02-18.
- [13] Marcelo Amaral, Jordà Polo, David Carrera, Seetharami Seelam, and Malgorzata Steinder. Topology-aware gpu scheduling for learning workloads in cloud environments. In *Proceedings of the International Conference for High Performance Computing, Networking, Storage and Analysis (SC)*, pages 1–12. ACM, 2017.
- [14] Jeongkyu Shin and Joongi Kim. Sokovan: Container orchestrator for accelerated AI/ML workloads and massive-scale GPU computing. Presented at OpenInfra Summit Vancouver, June 2023. Slides available at <https://www.backend.ai/ko/video/2023-06-11-openinfra-summit>.
- [15] NVIDIA Corporation. Dcgm-exporter: NVIDIA GPU monitoring tool for Prometheus. <https://github.com/NVIDIA/dcgm-exporter>, 2026. Accessed: 2026-02-15.
- [16] Prometheus Authors. Node exporter: Prometheus exporter for hardware and OS metrics. https://github.com/prometheus/node_exporter, 2026. Accessed: 2026-02-15.
- [17] Lablup Inc. all-smi: Cross-platform ai accelerator monitoring tool. <https://github.com/lablup/all-smi>, 2025. Accessed: 2026-02-05.
- [18] NVIDIA Corporation. NVIDIA GPU memory error management. <https://docs.nvidia.com/deploy/a100-gpu-mem-error-mgmt/index.html>, 2025. v590. Accessed: 2026-03-24.
- [19] John W. Young. A first order approximation to the optimum checkpoint interval. *Communications of the ACM*, 17(9):530–531, 1974.
- [20] John T. Daly. A higher order estimate of the optimum checkpoint interval for restart dumps. *Future Generation Computer Systems*, 22(3):303–312, 2006.
- [21] Leonardo Bautista-Gomez, Anne Benoit, Sheng Di, Thomas Herault, Yves Robert, and Hongyang Sun. A survey on checkpointing strategies: Should we always checkpoint à la Young/Daly? *Future Generation Computer Systems*, 161:315–328, 2024.
- [22] Juncheng Gu, Mosharaf Chowdhury, Kang G. Shin, Yibo Zhu, Myeongjae Jeon, Junjie Qian, Hongqiang Liu, and Chuanxiong Guo. Tiresias: A gpu cluster manager for distributed deep learning. In *Proceedings of the 16th USENIX Symposium on Networked Systems Design and Implementation (NSDI)*, pages 485–500. USENIX Association, 2019.
- [23] Wencong Xiao, Romil Bhardwaj, Ramachandran Ramjee, Muthian Sivathanu, Nipun Kwatra, Zhenhua Han, Pratyush Patel, Xuan Peng, Hanyu Zhao, Quanlu Zhang, Fan Yang, and Lidong Zhou. Gandiva: Introspective cluster scheduling for deep learning. In *Proceedings of the 13th USENIX Symposium on Operating Systems Design and Implementation (OSDI)*, pages 595–610. USENIX Association, 2018.

- [24] Aurick Qiao, Sang Keun Choe, Suhas Jayaram Subramanya, Willie Neiswanger, Qirong Ho, Hao Zhang, Gregory R. Ganger, and Eric P. Xing. Pollux: Co-adaptive cluster scheduling for goodput-optimized deep learning. In *Proceedings of the 15th USENIX Symposium on Operating Systems Design and Implementation (OSDI)*, pages 1–18. USENIX Association, 2021.
- [25] Suhas Jayaram Subramanya, Daiyaan Arfeen, Shouxu Lin, Aurick Qiao, Zhihao Jia, and Gregory R. Ganger. Sia: Heterogeneity-aware, goodput-optimized ml-cluster scheduling. In *Proceedings of the 29th ACM Symposium on Operating Systems Principles (SOSP)*, pages 642–657. ACM, 2023.
- [26] Pengfei Zheng, Rui Pan, Tarannum Khan, Shivaram Venkataraman, and Aditya Akella. Shockwave: Fair and efficient cluster scheduling for dynamic adaptation in machine learning. In *Proceedings of the 20th USENIX Symposium on Networked Systems Design and Implementation (NSDI)*. USENIX Association, 2023.
- [27] Sudarsanan Rajasekaran, Manya Ghobadi, and Aditya Akella. Cassini: Network-aware job scheduling in machine learning clusters. In *Proceedings of the 21st USENIX Symposium on Networked Systems Design and Implementation (NSDI)*. USENIX Association, 2024.
- [28] Arnab Choudhury, Yang Wang, Tuomas Pelkonen, Kutta Srinivasan, Abha Jain, Shenghao Lin, Delia David, Siavash Soleimanifard, Michael Chen, Abhishek Yadav, Ritesh Tijoriwala, Denis Samoylov, and Chunqiang Tang. Mast: Global scheduling of ml training across geodistributed datacenters at hyperscale. In *Proceedings of the 18th USENIX Symposium on Operating Systems Design and Implementation (OSDI)*. USENIX Association, 2024.
- [29] Qinlong Wang, Tingfeng Lan, Yinghao Tang, Ziling Huang, Yiheng Du, Haitao Zhang, Jian Sha, Hui Lu, Yuanchun Zhou, Ke Zhang, and Mingjie Tang. DLRouter-RM: Resource optimization for deep recommendation models training in the cloud. *Proceedings of the VLDB Endowment*, 17, 2024.
- [30] Mohammad Shoeybi, Mostofa Patwary, Raul Puri, Patrick LeGresley, Jared Casper, and Bryan Catanzaro. Megatron-lm: Training multi-billion parameter language models using model parallelism. *arXiv preprint arXiv:1909.08053*, 2019.
- [31] Deepak Narayanan, Mohammad Shoeybi, Jared Casper, Patrick LeGresley, Mostofa Patwary, Vijay Korthikanti, Dmitri Vainbrand, Prethvi Kasber, Matei Zaharia, and Bryan Catanzaro. Efficient large-scale language model training on gpu clusters using megatron-lm. In *Proceedings of the International Conference for High Performance Computing, Networking, Storage and Analysis (SC)*. ACM, 2021.
- [32] Yanping Huang, Youlong Cheng, Ankur Bapna, Orhan Firat, Mia Xu Chen, Dehao Chen, HyoukJoong Lee, Jiquan Ngiam, Quoc V. Le, Yonghui Wu, and Zhifeng Chen. Gpipe: Efficient training of giant neural networks using pipeline parallelism. In *Proceedings of the 33rd International Conference on Neural Information Processing Systems (NeurIPS)*, pages 103–112, 2019.
- [33] Samyam Rajbhandari, Jeff Rasley, Olatunji Ruwase, and Yuxiong He. Zero: Memory optimizations toward training trillion parameter models. In *Proceedings of the International Conference for High Performance Computing, Networking, Storage and Analysis (SC)*. IEEE, 2020.
- [34] Yanli Zhao, Andrew Gu, Rohan Varma, Liang Luo, Chien-Chin Huang, Min Xu, Les Wright, Hamid Shojanazeri, Myle Ott, Sam Shleifer, et al. Pytorch fsdp: Experiences on scaling fully sharded data parallel. *Proceedings of the VLDB Endowment*, 16(12):3848–3860, 2023.

- [35] Lianmin Zheng, Zhuohan Li, Hao Zhang, Yonghao Zhuang, Zhifeng Chen, Yanping Huang, Yida Wang, Yuanzhong Xu, Danyang Zhuo, Eric P. Xing, Joseph E. Gonzalez, and Ion Stoica. Alpa: Automating inter- and intra-operator parallelism for distributed deep learning. In *Proceedings of the 16th USENIX Symposium on Operating Systems Design and Implementation (OSDI)*, pages 559–578. USENIX Association, 2022.
- [36] Jayashree Mohan, Amar Phanishayee, and Vijay Chidambaram. Checkfreq: Frequent, fine-grained dnn checkpointing. In *Proceedings of the 19th USENIX Conference on File and Storage Technologies (FAST)*, pages 203–216. USENIX Association, 2021.
- [37] Tanmaey Gupta, Sanjeev Krishnan, Rituraj Kumar, Abhishek Vijeev, Bhargav Gulavani, Nipun Kwatra, Ramachandran Ramjee, and Muthian Sivathanu. Just-in-time checkpointing: Low cost error recovery from deep learning training failures. In *Proceedings of the Nineteenth European Conference on Computer Systems (EuroSys)*, pages 1110–1125. ACM, 2024.
- [38] Zhuang Wang, Zhen Jia, Shuai Zheng, Zhen Zhang, Xinwei Fu, T. S. Eugene Ng, and Yida Wang. Gemini: Fast failure recovery in distributed training with in-memory checkpoints. In *Proceedings of the 29th ACM Symposium on Operating Systems Principles (SOSP)*, pages 364–381. ACM, 2023.
- [39] Borui Wan, Mingji Han, Yiyao Sheng, Yanghua Peng, Haibin Lin, Mofan Zhang, Zhichao Lai, Menghan Yu, Junda Zhang, Zuquan Song, Xin Liu, and Chuan Wu. Bytecheckpoint: A unified checkpointing system for large foundation model development. In *Proceedings of the 22nd USENIX Symposium on Networked Systems Design and Implementation (NSDI)*. USENIX Association, 2025.
- [40] Insu Jang, Zhenning Yang, Zhen Zhang, Xin Jin, and Mosharaf Chowdhury. Oobleck: Resilient distributed training of large models using pipeline templates. In *Proceedings of the 29th ACM Symposium on Operating Systems Principles (SOSP)*, pages 382–395. ACM, 2023.
- [41] John Thorpe, Pengzhan Zhao, Jonathan Eyolfson, Yifan Qiao, Zhihao Jia, Minjia Zhang, Ravi Netravali, and Guoqing Harry Xu. Bamboo: Making preemptible instances resilient for affordable training of large dnns. In *Proceedings of the 20th USENIX Symposium on Networked Systems Design and Implementation (NSDI)*. USENIX Association, 2023.
- [42] Sanjith Athlur, Nitika Saran, Muthian Sivathanu, Ramachandran Ramjee, and Nipun Kwatra. Varuna: Scalable, low-cost training of massive deep learning models. In *Proceedings of the Seventeenth European Conference on Computer Systems (EuroSys)*, pages 472–487. ACM, 2022.
- [43] Baodong Wu, Lei Xia, Qingping Li, Kangyu Li, Xu Chen, Yongqiang Guo, Tiejiao Xiang, Yuheng Chen, and Shigang Li. TRANSOM: An efficient fault-tolerant system for training LLMs. *arXiv preprint arXiv:2310.10046*, 2023.
- [44] Yongji Wu, Wenjie Qu, Xueshen Liu, Tianyang Tao, Yifan Qiao, Zhuang Wang, Wei Bai, Yuan Tian, Jiaheng Zhang, Z. Morley Mao, Matthew Lentz, Danyang Zhuo, and Ion Stoica. Lazarus: Resilient and elastic training of mixture-of-experts models. *arXiv preprint arXiv:2407.04656*, 2024.
- [45] Jungsuk Kang and Joongi Kim. Method and apparatus for automatic recovery of tasks using execution failure-based resource requirement adjustment. Lablup Inc., 2026. Korean Patent Application 10-2026-0024429.

- [46] NVIDIA Corporation. cuDNN backend release notes. <https://docs.nvidia.com/deeplearning/cudnn/backend/latest/release-notes.html>, 2024. Cumulative release notes covering cuDNN 9.x; multiple FP8/MXFP8/NVFP4-related fixes across versions. Accessed: 2026-04-21.
- [47] Maxim Fishman, Brian Chmiel, Ron Banner, and Daniel Soudry. Scaling FP8 training to trillion-token LLMs. In *Proceedings of the Thirteenth International Conference on Learning Representations (ICLR)*, 2025. Spotlight. arXiv:2409.12517.
- [48] Joonhyung Lee, Jeongin Bae, Byeongwook Kim, Se Jung Kwon, and Dongsoo Lee. To FP8 and back again: Quantifying the effects of reducing precision on LLM training stability. *arXiv preprint arXiv:2405.18710*, 2024.

A System Architecture Details

This appendix describes the detailed implementation of the Backend.AI infrastructure summarized in Section 3. The core design of the Sokovan scheduler (two-level scheduling, NUMA-aware placement, gang scheduling) is covered in Section 3.3; here we describe the health check and storage architectures.

A.1 Multi-Layer Health Checks

Table 15 shows Backend.AI’s health check architecture.

Table 15: Multi-layer health check architecture

Layer	Mechanism	Timeout / Threshold
Infrastructure (etcd)	Periodic liveness probe	5.0 s
Infrastructure (Valkey/Redis)	Per-component ping	2.0 s per component, 5.0 s total
Infrastructure (PostgreSQL)	Periodic liveness probe	2–5 s
Agent RPC	Manager → Agent ping	5.0 s
Agent Liveness	Heartbeat + sweep	300 s timeout, 600 s sweep
Agent Status	Manager → Agent heartbeat	Default 40 s
Session Hang	Per-state allowed time	PREPARING: 1 h, TERMINATING: 30 min
GPU Hardware	PCI bus enumeration (<code>lspci</code>)	Rev <code>ff/00</code> = faulty
GPU Metrics	<code>all-smi</code> Prometheus endpoint	Thresholds in Alertmanager

A.2 Unified Storage Architecture

Backend.AI integrates storage into the session lifecycle through a proxy-based abstraction, uniformly exposing diverse storage backends (NFS, Ceph, cloud storage, etc.) as network volumes while applying quota and operational policies (Figure 18).

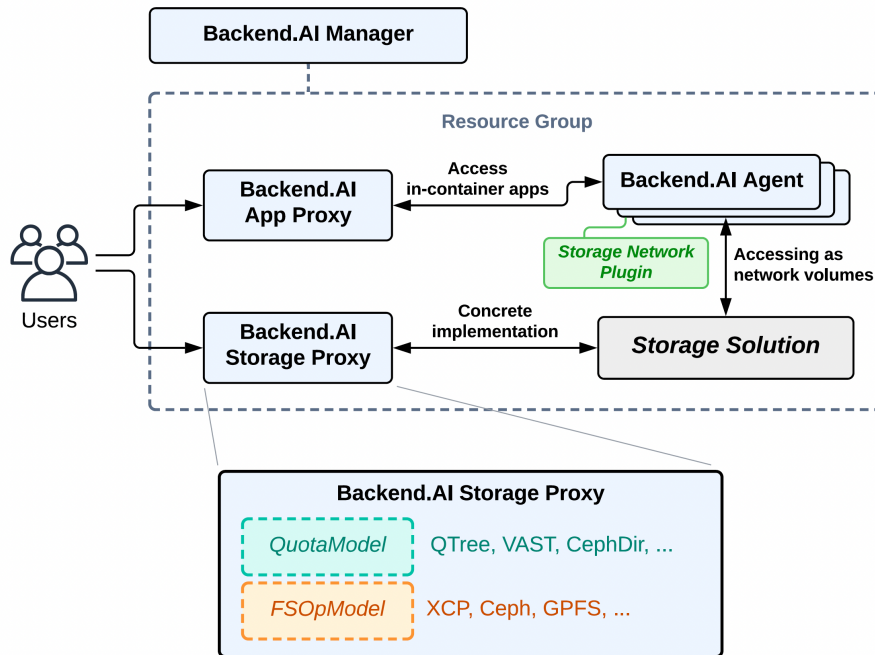


Figure 18: Backend.AI storage architecture and proxy-based integration. Storage resources are exposed to sessions as network volumes, with quota enforcement and filesystem operations managed by a system-level model.

B Glossary

Table 16: Terminology definitions

Term	Definition
Agent	Backend.AI’s per-node component that directly manages containers or virtual machines, allocates physical resources (GPU, CPU, memory), and reports status to the Manager
AOC	Active Optical Cable; an optical cable with optical-to-electrical conversion circuitry integrated at both ends. Used for longer node-to-switch links in GPU clusters where passive copper (DAC) length limits do not suffice
Auto-retry	Backend.AI FastTrack’s automated failure recovery mechanism that detects session failures and restarts sessions so the training framework can resume from the last checkpoint; supports configurable retry count and delay
cuDNN	CUDA Deep Neural Network Library; NVIDIA’s GPU-accelerated library of primitives for deep neural networks including convolution, normalization, and attention operations
DCGM	Data Center GPU Manager; NVIDIA’s suite of tools for monitoring and managing GPUs in cluster environments

Term	Definition
DGX	NVIDIA’s GPU server platform. This cluster comprises 63 DGX B200 nodes
ECC	Error-Correcting Code; a memory protection mechanism that detects and corrects bit errors. GPU ECC errors indicate hardware-level memory defects
etcd	A distributed key-value store used for service discovery and configuration management in cluster systems
FastTrack	Backend.AI’s MLOps orchestration layer that provides automated training management through auto-retry, session monitoring, and failure recovery workflows
FP8 / MXFP8	8-bit floating-point precision formats for training. FP8 reduces memory and compute costs; MXFP8 (Microscaling FP8) adds per-block scaling factors to improve numerical range
FSDP	Fully Sharded Data Parallel; a PyTorch distributed training strategy that shards model parameters, gradients, and optimizer states across workers
Gang Scheduling	All-or-nothing scheduling: either all required resources are allocated at once, or none are allocated at all
Goodput	The amount of useful training work completed per unit time, excluding overhead from checkpointing, communication latency, failure recovery, etc.
GSP	GPU System Processor; a RISC-V microcontroller running GPU firmware that communicates with the host driver via RPC. RPC timeouts are reported as XID 119
HBM	High Bandwidth Memory; stacked DRAM providing high-bandwidth, high-capacity memory for GPUs. HBM3e is the variant used in NVIDIA B200 GPUs (192 GB per device)
HDFS	Hadoop Distributed File System; the large-scale distributed file system of the Hadoop ecosystem. Block-based with a write-once-read-many model, optimized for big-data batch workloads
HSDP	Hybrid Sharded Data Parallel; a distributed training strategy combining FSDP sharding within node groups with data parallelism across groups
InfiniBand	A high-speed, low-latency interconnect fabric used for inter-node GPU communication in HPC and AI clusters. NDR denotes the 400 Gbps generation
IOPS	Input/Output Operations Per Second; a measure of storage system throughput for random access workloads
IQR	Interquartile Range; the range between the 25 th and 75 th percentiles, representing the middle 50% of a distribution
JCT	Job Completion Time
Manager	Backend.AI’s central control component that coordinates cluster-wide scheduling decisions, manages session lifecycle state, and communicates with Agents via RPC
MFU	Model FLOPs Utilization; the ratio of observed throughput to the hardware’s theoretical maximum FLOPS

Term	Definition
MoE	Mixture of Experts; a model architecture that activates only a subset of parameters per input token, enabling larger total model capacity at lower per-token compute cost
MTBF	Mean Time Between Failures
NCCL	NVIDIA Collective Communications Library; provides optimized collective operations (all-reduce, broadcast, etc.) for multi-GPU and multi-node training
NFS	Network File System; a distributed file system protocol enabling shared storage access across cluster nodes
NIC	Network Interface Card. This cluster provisions per-node InfiniBand NICs for GPU communication and separate RoCE NICs for storage traffic
NUMA	Non-Uniform Memory Access; a memory architecture in multi-socket systems where memory access latency varies depending on the relative position of CPU and memory
NVLink	NVIDIA's high-bandwidth interconnect for direct GPU-to-GPU communication within a node
OOM	Out of Memory; a runtime error that occurs when a process requests more memory (typically GPU memory) than is available
PCIe	Peripheral Component Interconnect Express; a high-speed serial bus connecting GPUs, NICs, and storage devices to the host
Prometheus	Open-source monitoring system for time-series metric collection and querying. The 751 metrics in this report were collected in Prometheus-compatible format and stored in VictoriaMetrics
Resource group	Backend.AI's logical partitioning unit for cluster resources. The scheduler treats each resource group independently to limit memory usage and isolate failures
RoCE	RDMA over Converged Ethernet; a network protocol implementing RDMA (Remote Direct Memory Access) over Ethernet. This cluster uses a dedicated 200 Gbps RoCE NIC for storage traffic
RPC	Remote Procedure Call; a communication mechanism for invoking functions in another process or host. Used for Manager-Agent communication in Backend.AI and client-server requests in NFS
Session	A logical training job unit in Backend.AI that can span multiple containers across multiple nodes, bundling storage, configuration, and lifecycle state as a single entity
Sokovan	Backend.AI's orchestration layer. Integrates session scheduling (NUMA-aware placement, gang scheduling), deployment management, and route management, reacting to events via a hint-based dual loop. This report focuses on the training session scheduling functionality
Temporal occupancy	The fraction of the observation period during which the cluster was occupied by training sessions, calculated as cumulative session elapsed time divided by the observation period

Term	Definition
XID	NVIDIA GPU error identifier; numeric codes reported by the GPU driver to classify hardware and software errors

C GPU Monitoring Dashboard

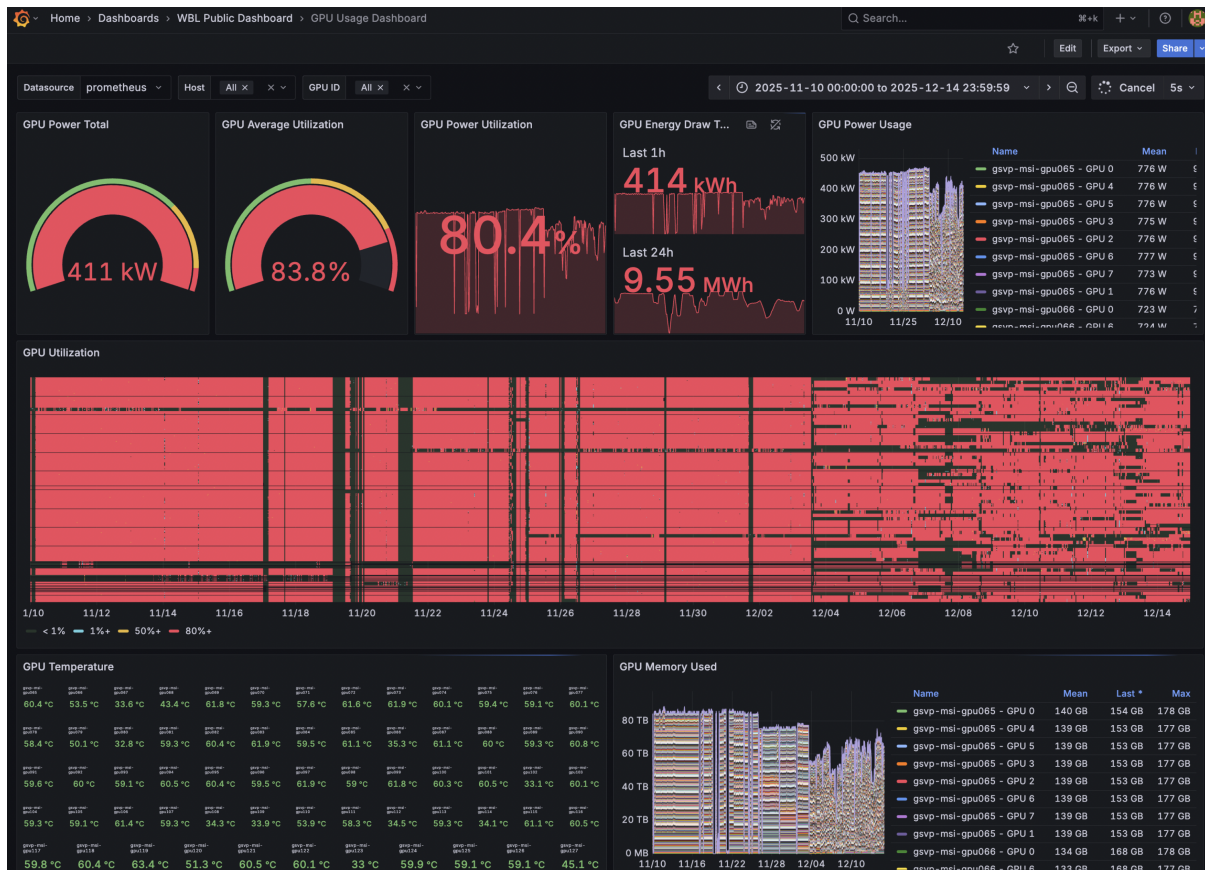


Figure 19: Grafana-based GPU monitoring dashboard deployed with Backend.AI. This dashboard provides real-time visualization of cluster-wide and per-node GPU power consumption, utilization, temperature, SM clocks, memory usage, and energy consumption, aggregating NVIDIA DCGM and `all-smi` metrics through Prometheus. This telemetry forms the observational basis for the failure analysis presented in Section 4.

D Author List

The following is a list of authors who contributed to the development and operation of Backend.AI and the infrastructure described in this report. Names are listed alphabetically by given name.

Daemyung Kang, Eunjin Hwang, Hanjeong Lee*, HyeokJin Kim, Hyunhoi Koo, Jeongkyu Shin, Jeongseok Kang, Jihyun Kang, Joongi Kim, Junbum Lee, Jungseung Yang, Kyujin Cho, Youngsook Song

*Work done during internship at Lablup Inc.